NASA TECHNICAL MEMORANDUM



NASA TM X-1128

ASA TM X-112

(ACCASION NUMBER)

(PAGES)

(PAGES)

(CODE)

(CATEGORY)

(PAGES)

(NASA CR OR TMX OR AD NUMBER)

(RECESSION NUMBER)

(CODE)

(CODE)

(CATEGORY)

EFFECT OF INTE AERODYNAMIC FLIGHT VELOCIT

by Ivan E. Beckwith Langley Research Ce Langley Station, Ha

NATIONAL AERONAUTICS AN

UNCLASSIFIED

MBER 1965





EFFECT OF INTERMITTENT WATER INJECTION ON AERODYNAMIC HEATING OF A SPHERE-CONE AT FLIGHT VELOCITIES

TO 18 000 FEET PER SECOND

By Ivan E. Beckwith and Dennis M. Bushnell

Langley Research Center Langley Station, Hampton, Va.

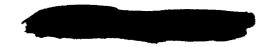
> GROUP 4 Downgraded at 3 year intervals; declassified after 12 years

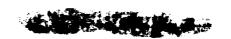
CLASSIFIED DOCUMENT-TITLE UNCLASSIFIED This material contains information affecting the national defense of the United States within the meaning of the espionage laws, Title 18, U.S.C., Secs. 793 and 794, the transmission or revelation of which in any manner to an unauthorized person is prohibited by law.

NOTICE

This document should not be returned after it has satisfied your requirements. It may be disposed of in accordance with your local security regulations or the appropriate provisions of the Industrial Security Manual for Safe-Guarding Classified Information.

NATIONAL AERONAUTICS AND SPACE ADMINISTRATION





TO SHEET BETTER AND ASSESSED.



EFFECT OF INTERMITTENT WATER INJECTION ON

AERODYNAMIC HEATING OF A SPHERE-CONE AT FLIGHT VELOCITIES

TO 18 OOO FEET PER SECOND*

By Ivan E. Beckwith and Dennis M. Bushnell Langley Research Center

SUMMARY

19129

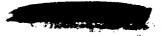
Temperature measurements obtained during the ascent flight of a 9° half-angle cone-cylinder vehicle (RAM B2) with a spherically blunted nose have been analyzed to determine aerodynamic heat-transfer rates. The data are in agreement with an integral theory for turbulent boundary layers up to an altitude of about 65 000 feet and a velocity of 4000 feet per second. Transition to laminar boundary layer then occurred, and the resulting value of minimum critical Reynolds number for transition was approximately 1×10^6 based on local flow conditions and distance from stagnation point.

Intermittent water injection was initiated at an altitude of 150 000 feet and a flight velocity of 14 000 feet per second. The first few injection cycles from the side ports caused a large cooling effect as far as 1 foot downstream of the injection site. An analysis of this cooling effect has been made by means of an approximate one-dimensional theory for water droplet motion and evaporation. At distances of less than 0.7 foot from the injection site, the results are in agreement with the data when the correlations of NACA TN 4087 for mean initial droplet diameter are used.

INTRODUCTION

The development of ablating materials for reducing aerodynamic heating and maintaining structural integrity of hypersonic vehicles has been very successful in the last few years. There are some situations, however, where active cooling systems become desirable or necessary. Examples of such situations would be when a given aerodynamic shape must be accurately maintained, or when the coolant must be injected beyond the nominal boundary layer to reduce radio attenuation caused by the plasma sheath which is present in the shock layer on a blunt body. In order to utilize the coolant efficiently, practical injection systems which will deliver the optimum amount of coolant in the desired region need to be developed. Methods for predicting the subsequent behavior and effectiveness of the coolant are also required.







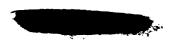
The first flight vehicle to use an active cooling system for the purpose of alleviating radio attenuation has been flown. This vehicle was designated RAM B2 and is one of a series in the RAM (Radio Attenuation Measurement) research program at the NASA Langley Research Center. Preliminary reports of the effect of the coolant, which was water, on radio transmission from the RAM B2 vehicle are available in references 1, 2, and 3. Details of the vehicle design and performance are given in reference 4.

Aerodynamic heating data from previous RAM flights are reported and analyzed in references 5 and 6. The vehicles used in these flights were 9° half-angle cone-cylinders with spherically blunted noses of 1-inch radius. The same basic shape was used for the RAM B2 vehicle, but the nose radius was increased to 4 inches.

The primary purpose of the present report is to present and analyze the aerodynamic heating data obtained during the RAM B2 flight, with particular emphasis on the effect of water injection and evaporation on surface heat transfer. A quantitative method for predicting the effect of water droplet evaporation on the laminar boundary layer is developed, and the results are compared with the experimental data on surface heating.

SYMBOLS

Α	area, or constant in drag coefficient equation						
$c_{\mathbb{D}}$	droplet drag coefficient						
$\frac{\mathrm{C_{p}}}{\mathrm{C_{p,max}}}$	pressure-coefficient ratio						
c	specific heat of metal or ablation materials						
$c_{\mathbf{p}}$	specific heat of air or gas mixture at constant pressure, energy per unit mass per $^{\mathrm{O}\mathrm{F}}$						
đ.	droplet diameter						
d _O	orifice diameter						
F	drag force						
fr	recovery factor						
fs	fraction of entering free-stream air cooled by spray (see eq. (A39))						
н	total enthalpy						
${\tt H_{eff}}$	effective heat of ablation						
2							



static enthalpy h h* heat-transfer coefficient thermal conductivity k latent heat of liquid L axial distance from stagnation point ı ī wall thickness M Mach number m mass flow rate number of orifices N droplet concentration N_{d} n exponent in drag-coefficient equation Nusselt number N_{Nu} Prandtl number N_{Pr} Stanton number, $\frac{h^*}{\rho u c_p}$ N_{St} pressure p heat-transfer rate per unit area q ratio of drop diameter to initial value, $\frac{d}{dt}$ R \overline{R} ideal gas constant, energy per unit mass reference Reynolds number, $\frac{\rho_t \sqrt{2H_e}r_N}{u_t}$ Rref droplet radius r nose radius of vehicle r_N surface distance downstream from injection orifices s temperature T t time



 Δt_1 initial response time of ablation material (see eq. (4))

u velocity

V relative velocity between gas and droplets, um - ud

$$W^* = \frac{\dot{m}_C}{\dot{m}_B}$$

$$\overline{W} = \frac{\dot{m}_V}{\dot{m}_{a}}$$

X mole fraction

x surface coordinate with origin at stagnation point

y coordinate normal to surface

 α thermal diffusivity, $\frac{k}{\rho c}$

β similarity parameter (see ref. 17)

 γ ratio of specific heats

η total angle of attack, or similarity boundary-layer coordinate (see ref. 14)

 μ coefficient of viscosity

ρ density

σ surface tension of liquid

p angular displacement around vehicle (see fig. 3)

Subscripts:

a air

ab ablation

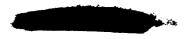
aw adiabatic wall

cw cold wall

c coolant

4

C continuum applied to C_{D} or N_{Nu}



đ	droplet
е	external to boundary layer
f	film
FM	free molecule
i	initial value
7	injected liquid
m	mixture of air and vapor
0	zero mass transfer
sat	saturation point of liquid or vapor
t	stagnation point on vehicle
v	vapor
W	wall or surface of vehicle
1	initial value at injection point
∞	free stream ahead of bow shock

APPARATUS

Launch Vehicle

The launch vehicle was an unguided, three-stage configuration with solid-propellant rocket motors. It was designed to place a 175-pound payload on an ascending trajectory at an altitude of 180 000 feet with a velocity of about 20 000 ft/sec. The first and second stages consisted of the Castor-E8 and Antares-IAl rocket motors, respectively, and were fin stabilized. The third stage consisted of a 30 KS 8000 (Alcor) rocket motor and the test vehicle, which was flare stabilized. Complete details of the rocket motors and construction of the launch vehicle are given in reference 4.

Test Vehicle

The test vehicle, or payload, was a 9° half-angle cone-cylinder-flare configuration with a spherically blunted nose of 4-inch radius. The maximum diameter of the cylindrical section was 22.25 inches. The total length of the vehicle including the 13° half-angle flare was 138.2 inches. In order to provide a clean environment for the water injection, the forward portion of the





vehicle consisted of a beryllium shell that varied in thickness from 1.5 inches at the stagnation point to 0.16 inch at its downstream end. The streamwise, or axial, length of this beryllium heat sink was 18.81 inches. The remainder of the vehicle was protected by a noncharring ablation material. (See ref. 7.) The properties of the ablation material as used in the present report are listed in table I. A complete description of the vehicle including the interior layout and construction detail is given in reference 4.

Injection Orifices

The injection system was designed to place a liquid spray throughout the inviscid shock layer. The vehicle was provided with three injection sites: one at the stagnation (or nose) region and two on opposite sides of the conical portion about 1.3 inches aft of the sphere-cone junction. The injection site at the stagnation region had 6 orifices arranged in a circular pattern with 1 at the center for a total of 7 orifices, all of 0.08-inch diameter. Each side injection site had 14 separate nozzle stations with 7 orifices at each station for a total of 98 orifices, all of 0.015-inch diameter. Figure 1 is a photograph of the beryllium nose section showing the injection orifices at the stagnation region and the injection nozzle stations on one side of the cone. Also visible in this photograph are the differential pressure ports used to sense angle of attack as described in reference 4.

The detailed layout and dimensions of the injection sites and orifices are given in figure 2. The side nozzles were arranged in a lateral pattern that extended 49° around the side of the vehicle with 3.5° angular spacing between each nozzle site as indicated in the figure. The side nozzles were installed so that their center-line axes were perpendicular to the local surface of the vehicle. The nose nozzles were installed so that their center-line axes were parallel to the axis of the vehicle.

A rotary distribution valve was used to vary the mass flow and the on and off sequence during an injection cycle by opening the appropriate number of nozzles to the pressurized storage tank. The cycle was repeated continuously starting at 110 seconds from launch and lasting until the water supply of 22 pounds was exhausted. A cycle consisted of an injection period of 2 seconds from the stagnation nozzles, an off period of 1 second for attenuation calibration purposes, and an injection period of 2 seconds from both side sites simultaneously, followed by another off period of 1 second. (These times are nominal; the actual injection and off periods varied from the nominal values by 0.1 to 0.2 second due to fill and bleed times of the plumbing.) During the injection periods the flow rate was varied through seven levels for both the stagnation and side nozzles. A more detailed description of the injection system and its operation is given in reference 1.

Thermocouple Installation

A total of 21 thermocouples were attached at various points on the vehicle. The present report is concerned only with data from 11 of these thermocouples:





5 that were attached to the beryllium nose portion and 6 that were attached to the aluminum skin, which supported the ablation material. The thermocouple junctions were made by spot welding the individual wires about 0.06 inch apart to the inside surface of the beryllium shell or aluminum skin. Chromel-alumel wire of 0.01-inch diameter was used on the beryllium nose, and iron-constantan wire of the same diameter was used on the aluminum skin.

The locations of the thermocouples used in the present report and the corresponding structure or skin thicknesses are given in figure 3, which is a side-view sketch of the forward portion of the vehicle. Note that thermocouples 2, 4, and 5 are directly downstream of a side injection site at $\phi = 270^{\circ}$, whereas thermocouples 1 and 3 are at $\phi = 0^{\circ}$, which is 90° from the center of the side injection sites.

Figure 4 is a sectional drawing of the beryllium nose cone and shows the location of joints and flanges in relation to thermocouple locations. Due to the high thermal conductivity of beryllium, these joints and flanges would be expected to have some effect on temperature in their vicinity. The thermal conductivity and heat capacity of beryllium were taken from reference 8. The density of beryllium was taken as 114 lb/ft^3 .

The output of each thermocouple was sampled at a rate of 3 times per second by commutating switches. Real-time data were transmitted from the 225.7-Mc telemetry system, and an 80-second delayed playback signal was transmitted from the 244.3-Mc telemetry system. Thus, in case of loss of signal due to blackout, complete telemetry coverage was provided after the vehicle emerged from blackout conditions. Further details on vehicle instrumentation, transmitting and recording equipment, range stations, and so forth, are given in reference 4.

TEST CONDITIONS

Trajectory

The RAM B2 vehicle was launched on May 28, 1963, at 2:59:09 p.m. e.d.t. from the NASA Wallops Station. The trajectory was designed to penetrate the blackout region during the ascent when the vehicle was within range of coastal land and off-shore ship receiving stations. The ascent portion of the trajectory was thereby the primary data period, and it was unnecessary to design the vehicle to survive the more severe reentry heating conditions.

The principal trajectory parameters of interest in the present investigation are plotted against time from launch in figure 5. These parameters are based primarily on smoothed radar data as discussed in detail in reference 4. Ignition and burnout times are also shown in figure 5. The peak velocity was almost $18\,000\,$ ft/sec at third-stage burnout, which occurred at an altitude of $163\,000\,$ feet (fig. 5(a)). The Reynolds number based on free-stream conditions reached a peak value of $1.05\times10^7\,$ per foot (fig. 5(b)) during first-stage burning. These large Reynolds numbers together with the size of the vehicle indicate that turbulent boundary-layer heating would probably be present during





this portion of the flight. The peak Mach number (fig. 5(c)) of 20.5 was reached at a time of about 190 seconds when the altitude was 263 000 feet.

Angle of Attack

Envelope curves of the maximum and minimum angle of attack obtained from reference 4 are plotted against time from launch in figure 6. Up to the beginning of water injection at 110 seconds the angle of attack was less than 2° except for a period of 5 seconds after second-stage ignition. Since the vehicle was spinning at a rate of about 3 rps (ref. 4), this angle of attack would not have any significant effect on aerodynamic heating.

After 110 seconds, however, the angle of attack appears to diverge to increasingly large values until at 150 seconds it varied from about 0.5° to 7°. The blank regions in the data after 110 seconds occurred during stagnation injection when flow field variations or the presence of water near the sensing ports prevented valid readings. It is possible that the data which are shown during the remainder of the injection period may be affected by residual water within the pressure instrument cavity or pressure ports. Even if the large angle-of-attack excursions indicated in figure 6 actually occurred, they probably did not have large effects on temperature data, since the vehicle spin would tend to average out temperature variations because of the large heat capacity of the structure.

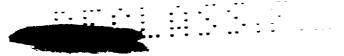
Pressure Distributions and Local Flow Conditions

The local surface pressures which were required in the boundary-layer solutions used in the present investigation were obtained from reference 9. The results of reference 9 are based on inviscid-flow-field solutions for sphere-cones by the method of reference 10. Typical distributions of the surface-pressure coefficient are shown in figure 7(a). A 9° Prandtl-Meyer expansion at the cone-cylinder junction $(x/r_N = 12.87)$ would reduce the pressure coefficient ratio to 0.0086. This value was then assumed constant from the junction to the downstream thermocouple station.

The variation with free-stream Mach number of the normalized pressure coefficient at the five thermocouple stations on the beryllium nose section is shown in figure 7(b). The variation of Mach number with altitude indicated in this figure corresponds roughly to the RAM B2 trajectory; hence, these values of normalized pressure coefficient are used in all subsequent calculations for these stations.

With the local pressure known, the local velocity, density, and temperature at the edge of the boundary layer can be computed by assuming an isentropic expansion from the stagnation point. Stagnation-point entropy was obtained from the normal-shock tables of reference 11. This entropy and the total enthalpy were then used to determine all other stagnation-point conditions from the equilibrium air properties of reference 12 which was also used for the isentropic expansion.





Resulting values of the local Reynolds number at the five thermocouple stations on the beryllium nose are shown in figure 8(a). The length used in the local Reynolds number is the distance along the surface from the stagnation point, and the viscosity is computed from Sutherland's formula. The large Reynolds numbers during the first 50 seconds of the flight indicate again that turbulent heating can be expected during this time.

The local Mach number for these five stations is plotted in figure 8(b). Both the local Mach number and Reynolds number are parameters of interest in connection with the possibility of transition from laminar to turbulent (or vice-versa) flow in the boundary layer.

Water Flow Rates and Efflux Velocities

Water injection was initiated at 110 seconds after launch by a squib valve between the supply tank and the rotary distribution valve. The distribution valve was set in operation at launch and was rotated at a constant speed of 1 revolution in 6 seconds. The duration of one injection cycle was thus approximately 6 seconds. When the squib valve fired, the rotary valve was part way through a side injection cycle.

The total water flow rate is plotted against time in figure 9. The data shown in this figure were actually obtained from a preflight calibration for which all pertinent flight conditions were duplicated as close as possible. These conditions were: the supply-tank pressure, exit pressure, rotary-valve speed, and vehicle spin rate.

Note that seven distinct levels of flow are evident for each stagnation and side injection period up until the stagnation injection period at about 162 seconds when only 4 levels can be distinguished. This same change in massflow variation was observed during several calibrate runs and was believed to be caused by a partial malfunction of the diaphragm in the supply tank. Since the change occurred near the end of the injection period and appeared to be reasonably repeatable, no modifications to the injection system were made and it was assumed that the observed variation also occurred in flight.

The integral of the flow-rate curve of figure 9 is 21.5 pounds as compared with the total of 22 pounds of water initially loaded in the tank. The onboard measurement indicated some slight changes in tank pressure out to about 200 seconds. Apparently, the approximately 0.5 pound of water remaining after 180 seconds was discharged in the succeeding 20 seconds.

In order to obtain estimates of the ratio of mass flow rate of water to mass flow rate of air, W*, in the mixing region, it is necessary to determine the maximum penetration of the water spray. In reference 13 the maximum penetration of a liquid spray for cross-current injection was correlated in terms of the free-stream density and velocity and the efflux velocity and density of the liquid. The variation of efflux velocity for injection from the side orifices during the RAM B2 flight is shown in figure 10. These velocities were computed for the maximum and minimum mass flow rates by using the data from





figure 9 and the corresponding total exit area of the orifices. That is, for the maximum mass flow, all 28 nozzle stations on both sides were in operation for a total of 196 orifices. For the minimum flow rate, 4 nozzle stations, or 28 orifices, were in operation. The velocities are slightly larger for the smaller mass flow due to the smaller losses in the system. An idea of the total losses in the system can be obtained by comparing the previously discussed results with the velocity computed directly from the tank pressure with the assumption of no losses.

ACCURACY

The level of the measured temperatures is considered to be accurate to within ± 2 percent of a full-scale reading. This percentage error results in an absolute error of $\pm 40^{\circ}$ F for the chromel-alumel thermocouples used on the beryllium nose and $\pm 20^{\circ}$ F for the iron-constantan thermocouples on the aluminum skin. The accuracy of an indicated temperature reading from any one thermocouple in relation to other readings during its time history is much better than this and depends mainly on the sensitivity of the telemetry system, the response time of the instrument system, and the sampling rate of the commutating switch. The response time of the instruments is better than 1 millisecond and the sampling rate of the commutating switch was 3 readings per second per thermocouple. The capability to detect any cyclic variation in temperatures is thus limited by the sampling rate and the thermal response time of the structure where the thermocouple is attached. Typical random data scatter for a monatonic increase in temperature indicates that the relative accuracy is about $\pm 5^{\circ}$ F for any particular chromel-alumel thermocouple.

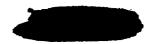
The main concern in the present report in regard to accuracy is the thermocouple instrumentation system. However, the accuracy of trajectory parameters is also important, particularly the altitude. Information concerning the accuracy of the trajectory data, as well as vehicle motion, is available in reference 4.

HEATING PREDICTIONS

Laminar

Stagnation point. The stagnation-point heating rate is a convenient reference value for the laminar heat-transfer distribution on the rest of the vehicle and was computed from the correlation of reference 14. This correlation applies directly to spherically shaped noses and depends only on the flight velocity and altitude.

The computer program of reference 15 was used to compute wall temperatures for the stagnation point and all thermocouple stations considered in this report. This program uses as input the "cold wall" heating rate $\, q_{cw} \,$ and, by iteration, determines the response of the wall structure in order to calculate





the final wall temperature and the final aerodynamic heating rate $\, q_{W}, \,$ where it is assumed that

$$\frac{\mathbf{q}_{\mathbf{cw}}}{\mathbf{H}_{\mathbf{aw}}} = \frac{\mathbf{q}_{\mathbf{w}}}{\mathbf{H}_{\mathbf{aw}} - \mathbf{h}_{\mathbf{w}}}$$

As an example of this computing procedure, the input values of q_{cW} and the values of q_w obtained from the program for the stagnation point are shown in figure 11. Peak heating occurs at 120 seconds at an altitude of 165 000 feet and a velocity of 18 000 ft/sec. At early times in the flight, before 100 seconds, there are large differences in q_{cW} and q_w because h_w/H_{aW} is still appreciable. For times greater than 100 seconds when $M_\infty > 10\,$ the values of q_{cW} and q_w are approximately the same since $\frac{h_W}{H_{aW}} \ll 1.$

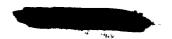
The surface temperatures obtained from the calculation for the stagnation point are shown in figure 12. The outside surface temperature peaks at about 160 seconds or 40 seconds after peak heating. The inside surface temperature lags the value at the outside by a maximum of 675° F which occurs at peak heating. These large differences between the inside and outside temperatures are caused by the large wall thickness which was 1.5 inches at the stagnation point.

Distribution. The theoretical distribution of laminar heat-transfer coefficient along the surface of the sphere-cone portion of the body is shown in figure 13. The local similarity theories of references 16 and 17 were used to compute the ratios h^*/h_t^* as shown in the figure. The method of reference 17 allows for a change in the enthalpy profile along the body; whereas, the method of reference 16 assumes this profile to be invariant. The effect for the present configuration is seen to be small. The nominal conditions used in the calculation (as given in fig. 13) are close enough to the flight conditions during the latter portion of the trajectory so that the effect on h^*/h_t^* would be negligible. The h^*/h_t^* distribution computed by the method of reference 17 was used in subsequent calculations for wall temperature during the laminar heating period.

The heat transfer just downstream of the cone-cylinder junction is reduced to about 1/2 the value on the cone. This decrease in heat transfer depends only on the reduction in pressure which was given in figure 7(a).

Turbulent

Turbulent heating rates were computed by two methods. One of these is a "local flat plate" method based on a modification of Falkner's skin-friction formula (ref. 18) and Reynolds analogy. The resulting expression for heating rate is





$$q_{w} = \frac{0.0157\rho_{w}u_{e}(H_{aw} - H_{w})}{\left(\frac{\rho_{u}u_{e}X}{\mu_{w}}\right)^{1/7}}$$
(1)

This expression has the advantage of being very simple to apply and was found to be in good agreement with experimental turbulent heating rates on blunt bodies at stream Mach numbers of about 4 or less (refs. 19 to 21).

The other method used for computing turbulent heating is that of reference 22. This method is based on the complete solution of the boundary-layer integral equations which are transformed to a quasi-incompressible form. Power-velocity profiles and a Colburn type skin-friction law based on momentum thickness are used in the transformed equations. Because of the form of the skin-friction law and other assumptions used in this theory, the quantity

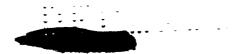
$$N_{St} \left(R_{ref}\right)^{1/5} = \frac{q_w}{\rho_e u_e \left(H_{aw} - H_w\right)} \left(\frac{\rho_t \sqrt{2H_e} r_N}{\mu_t}\right)^{1/5} \tag{2}$$

is independent of Reynolds number and depends mainly on the pressure distribution, and to a lesser extent on the flight Mach number, wall temperature, and the ambient temperature. This quantity is plotted against x/r_N in figure 14 as computed from the theory of reference 22. The nominal conditions used in the calculation are given in the figure.

Also plotted in figure 14 is the variation of $N_{\rm St}(R_{\rm ref})^{1/5}$ as obtained from the local flat plate method computed by equation (1). Since the Reynolds number dependence of equation (1) is different from the theory of reference 22, a comparison between the two methods is valid only if the Reynolds number is specified. The value of $R_{\rm ref}$ chosen for this purpose was 3.4 \times 100 which occurs at a time of about 40 seconds from launch for the RAM B2 flight. (During the time interval from 20 to 50 seconds the curve shown would not vary more than from 7 to -4 percent as the Reynolds number decreases from its peak value.)

The maximum difference between the predictions of the two methods occurs at the sphere-cone junction ($x/r_N=1.41$) where the integral method of reference 22 predicts heating about 40 percent lower than the value for local flat plate theory. Most of this difference is due to the effect of pressure gradient which is the greatest at this location. Farther downstream, near the conecylinder junction, the integral method gives heating about 15 percent lower, presumably because the skin-friction law used in the integral method is based on the momentum thickness and thus would account more properly for previous boundary-layer history than does the local flat plate method. In the vicinity of the thermocouples from $x/r_N=2.02$ to $x/r_N=4.80$ the results from the





integral method average about 25 percent less than those from the local flat plate method.

RESULTS AND DISCUSSION

Temperature-Time Histories for Zero Injection and

Transition on Beryllium Nose Section

Measured temperatures. Temperature-time histories on the beryllium nose section are shown in figure 15. The solid line curves are faired from telemetered data as obtained for the five thermocouples (figs. 15(a) to 15(e)) attached to the inside surface. The dashed line curves were computed from theoretical heating rates and will be discussed in a subsequent section.

During the first 40 seconds of the flight, the temperatures at all thermocouple stations increase rapidly. This portion of the trajectory is during the first-stage boost when the velocity is increasing to a peak of 4000 ft/sec but the altitude is less than 50 000 feet. The free-stream Reynolds number reaches its peak of 107 per foot at about 25 seconds; therefore, there is a possibility that turbulent heating occurred during this period of the flight.

Transition as indicated by heating rates. Experimental heating rates have been estimated by assuming the beryllium shell behaves as a simple calorimeter; that is, the aerodynamic heating rate is assumed proportional to the indicated temperature-time derivative according to the relation

$$q_{w} = \rho c \overline{l} \frac{dT_{w}}{dt}$$
 (3)

Heating rates computed in this manner from the faired temperature data of figure 15 are plotted against time from launch in figure 16. Also plotted in figure 16 are predicted heating rates as computed from the turbulent and laminar theories described previously.

Up to about 35 seconds the data are in best agreement with the integral turbulent theory of reference 22, although at peak heating (30 seconds) the data are still from 20 to 30 percent below the theory. Between 50 and 60 seconds the data tend to approach the laminar theory (except for thermocouple 1) and from 60 seconds to 110 seconds (the start of water injection) the data are in good agreement with laminar theory. It is thus apparent that the boundary layer changed from turbulent to laminar, more or less simultaneously at thermocouples 2 to 5 in the time interval from about 50 to 55 seconds. By referring to figures 8(a) and (b) it is seen that for these thermocouple stations, this time interval corresponds to a local Reynolds number range from about 0.8 \times 106 to 1.5 \times 106 and local Mach numbers from 2.18 to 2.35. From a comparison of the data and theory of figure 16(a) for thermocouple 1, it is possible to conclude that transition occurred a little earlier at this station, possibly at





45 seconds. This time corresponds to a local Reynolds number of 1×10^6 and a local Mach number of 2.15 for this station.

Since the observed transition was from an established turbulent boundary layer to a laminar boundary layer, it is apparent that these Reynolds numbers are minimum critical values for transition at the local conditions of Mach number and wall temperature. (From fig. 15 and the known trajectory conditions. the ratio of wall temperature to stagnation temperature was about 0.64 at 50 seconds.) That is, for the particular body shape investigated and wall temperature a turbulent boundary layer could not exist at any lower Reynolds number. This conclusion is further substantiated by possible effects of angleof-attack disturbances associated with second-stage ignition at 51 seconds as indicated by figure 6. These disturbances would tend to maintain a turbulent boundary layer as long as possible. It is therefore concluded that the minimum critical Reynolds number for transition based on local conditions and length of flow from the stagnation point is 1×10^6 for this type of body shape. (This value is based on the assumption that transition occurred at 50 seconds for thermocouples 2 to 5 and at 45 seconds for thermocouple 1.) The corresponding local Mach number is 2.2, and the ratio of wall temperature to stagnation temperature is 0.64.

Aerodynamic heating data obtained on the RAM Al and RAM A2 vehicles are reported in references 5 and 6. The nose portion of these vehicles was the same shape as that of the RAM B2 but had a radius of 1 inch. The velocityaltitude trajectories of these vehicles were similar to that of the RAM B2. Transition from initially turbulent boundary layer to laminar boundary layer was also observed in these flights. In reference 5, the transitional Reynolds numbers based on local flow conditions and surface distance from the stagnation point varied from 0.9×10^6 to 1.6×10^6 at a local Mach number of about 2.80. These transitional Reynolds numbers are in good agreement with the present values and can probably also be considered minimum critical Reynolds numbers.

No transition Reynolds numbers were reported in reference 6; however, the data indicate that transition occurred at roughly the same stream conditions as in reference 5 so about the same values of transition Reynolds numbers would be expected.

Comparison of predicted and measured temperatures. Temperature-time histories on the beryllium nose for zero water injection were computed by using the numerical method of reference 15. The resulting values for the inside surface temperatures are plotted in figure 15. The local flat plate theory (eq. (1)) was used for the turbulent heating rates up to transition which, for the present purpose, was assumed to occur at all stations at 50 seconds. From this time on, laminar heating rates were used as described previously.

The agreement between the computed temperatures and the faired telemetry data (fig. 15) is good up to about 35 seconds, or about 5 seconds past peak turbulent heating rates. After 35 seconds the computed temperatures are higher than measured values. Part of this discrepancy is probably caused by the theoretical heating rates being too large as shown by figure 16. Another reason for the discrepancy may be the conduction of heat into the flanges and joints



on the beryllium nose. This heat conduction is not accounted for by the simple calorimeter equation used. From the sectional drawing of figure 4, the heat conduction losses would be expected to affect thermocouples 1, 2, and 5 more than thermocouples 3 and 4. Examination of figure 15 shows that from 35 to 110 seconds the measured temperatures at thermocouples 1, 2, and 5 (figs. 15(a), (b), and (e)) are a maximum of 105°, 50°, and 45° below the predicted temperatures, whereas at thermocouples 3 and 4 (figs. 15(c) and (d)), the temperatures are at most 35° below the predicted values. It is thus apparent that at least some of the discrepancy between the measured and computed temperatures is due to heat conduction into the flanges and joints. Also, the observed decrease in temperature at thermocouple 1 during the time interval from 45 to 60 seconds can only be explained by heat conduction into the nearby joint, since the predicted local aerodynamic heating is still positive during this time according to figure 16(a).

Temperatures on Part of Cone-Cylinder Covered by Ablator

Measured and predicted temperatures at typical thermocouple stations on the inside surface of the aluminum and ablator composite wall are shown in figure 17. The predicted temperatures were obtained from the computer program of reference 15 with the ablator layer divided into 20 uniform step thicknesses, but with the aluminum skin treated as a heat sink of uniform temperature. The heat input rates used in the calculation were determined in the same manner as in the computation of the beryllium temperatures of figure 15 as described in the previous section. The material properties of the ablator and the expression for the heat of ablation as used in the computation are listed in table I. The material properties used for the aluminum skin were: ρ = 0.101 lb/in. 3 and c = 0.22 Btu/lb- $^{\circ}F$.

The measured temperatures are within about 25° F of the predicted values until after 110 seconds plus the initial response time Δt_1 . This initial response time was computed from the equation

$$\Delta t_{1} = \frac{1}{12} \frac{\overline{l}_{1}^{2}}{\alpha} \tag{4}$$

where \bar{l}_1 is the initial thickness of the ablator material. The factor of 1/12 was obtained by assuming a cubic temperature profile in the material, which is treated as a semi-infinite slab with boundary conditions appropriate to a step input of heat at time zero. The time Δt_1 then corresponds to the arrival of a finite temperature increase at the depth of \bar{l}_1 . It follows that any change in heat input conditions at the exterior surface is not sensed at the inside surface until Δt_1 seconds later. It is therefore apparent that the increasing discrepancy between the measured and computed temperatures that occurs at approximately $110 + \Delta t_1$ seconds as indicated at thermocouples 6, 12, and 16 (figs. 17(a), (b), and (c), respectively) is caused by the cooling effect of water injection which was initiated at 110 seconds. The predicted temperatures were computed for zero injection.



Another feature to be noted in the data of figure 17 is the apparent smaller response time indicated at thermocouple 6 (fig. 17(a)) as compared to either the value from equation (4) or from the temperature curve, computed by the "exact" numerical method of reference 15. This indicated response time appears to be smaller than Δt_i for the first temperature rise at about 30 seconds and also after the start of water injection as indicated by the "knee" in the faired data curve at about 140 seconds. The good agreement between the predicted and measured response times at the other two stations as shown in figures 17(b) and (c) indicates that the value used for thermal diffusivity is correct. If the thermal diffusivity is correct then it seems likely that some of the ablation material was lost in the vicinity of thermocouple 6 early in the flight, during the first 10 or 20 seconds.

In order to determine how much material may have been lost, the preflight thickness at the five thermocouple stations is compared in figure 18 with an effective thickness, which was defined as

Effective thickness =
$$\sqrt{12\alpha(\Delta t)_{10}}$$

The quantity $(\Delta t)_{1}^{\circ}$ is the time required for a thermocouple to show an increase of 1° F (according to faired telemetry data) above the temperature at time zero. According to the figure, almost 0.1 inch of material was apparently lost at thermocouple 6 as compared with little or no loss of material at the other five stations.

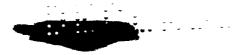
The predicted reduction in material thickness $\Delta \bar{l}$ due to the normal ablation process is shown in figure 19. The change in thickness due to this effect would certainly be less than 0.00l inch during the first heat pulse.

The reason for the indicated excessive loss of material at thermocouple 6 is unknown. It is possible that some flow disturbance upstream caused a large increase in local heating. However, it seems more likely that the large shear or pressure forces during the first 10 to 30 seconds (when the dynamic pressure was near 6000 lb/ft² (ref. 4)) caused a localized failure of the material. Such a failure may have started near the plugs (fig. 4) used to fill bolt holes in the ablation material provided for assembly of the nose-cone structure to the vehicle. A cross section of such a typical plug is shown in figure 4, and the location of the plug nearest thermocouple 6 is also indicated.

Effect of Water Injection on Temperatures and Heating Rates

Gross effects.— A qualitative indication of the different effect of side and nose injection on heat transfer to the vehicle surface can be obtained by comparing the faired temperature histories of thermocouples 2 and 4 (figs. 15(b) and (d)) with those of thermocouple 3 (fig. 15(c)). At the end of the injection period (about 200 seconds from launch), the temperatures at the former thermocouples are less than the temperatures at the latter thermocouple by about 200° F and 100° F, respectively. Since thermocouples 2 and 4 were





directly downstream of the side injection sites and thermocouple 3 was displaced 90° laterally from the side sites (fig. 3), it is apparent that the reduced temperatures at thermocouples 2 and 4 were caused by the relatively greater cooling effect of side injection as compared with nose injection.

Also note that thermocouple 2 (fig. 15(b)), which was about 5 inches downstream of the side injection site, indicated a marked decrease in temperature beginning at 120 seconds or shortly after the start of injection. Figure 11 shows that peak heating occurred at 120 seconds, so this reduction in temperature would represent a large cooling effect of the side injection. Thermocouples 4 and 5 are farther downstream from the side site and the faired data did not indicate any actual decrease in temperature due to injection at these stations.

A quantitative indication of the magnitude of the cooling effect can be obtained by comparing the measured and computed temperatures after the start of water injection (at 110 seconds) as shown in figure 15. The computed temperatures in this figure are for the case of zero injection. Temperatures read from this figure are listed in the following table, where subscript c is used to denote a computed temperature and subscripts 1 and 2 are used for temperatures at 110 and 200 seconds, respectively.

Thermo-couple	ø, deg	Figure	T ₁ ,	T _{1,c} ,	T ₂ , o _F	T2,c,	T _{2,c} - T ₂ , o _F	T _{2,c} - (T _{1,c} - T ₁) - T ₂ , o _F
1	0	16(a)	535	628	832	1080		155
2	270	16(b)	585	645	592	1060		408
3	0	16(c)	601	638	795	1046		214
4	270	16(d)	598	632	683	1016		299
5	270	16(e)	580	633	705	995		237

The last two columns on the right provide a direct measure of the cooling effect. The first of these columns is the difference between the computed and measured temperatures at the end of the injection period (approximately 200 seconds). The apparent effect of water injection was a reduction in all temperatures by at least 250° F.

A more realistic estimate of this temperature reduction can be obtained by adjusting the theoretical temperature curves for the loss of heat due to conduction into flanges and joints. This adjustment was made, somewhat arbitrarily, by subtracting the difference between computed and measured temperatures at 110 seconds from the computed values at 200 seconds. The result is shown in the last column on the right. The temperature decrease caused by the cooling effect of water injection then varies from 155° F to 408° F with the largest values occurring for stations at $\emptyset = 270^{\circ}$, which are directly downstream of the side injection ports. The actual amount of heat removed by the water thus varied from about 240 Btu/ft² to 470 Btu/ft² during the 90 seconds duration of injection. These values were computed from the appropriate values

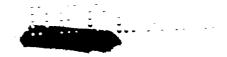


of beryllium thickness, specific heat, density, and temperature differences corresponding to thermocouple positions 1 and 2.

The smaller cooling effectiveness of stagnation injection as compared with side injection may be due to several different reasons. One of these reasons would be that for a given coolant flow rate, the resulting coolant concentration for nose injection would be less than that for side injection, since the same amount of coolant would be distributed over the entire flow field rather than just a portion of it as in the latter case. This effect was noted in the wind-tunnel tests of reference 13 where approximately eight times more coolant had to be injected at the nose to get the same local cooling effect as with side injection. Another possible reason for the smaller effectiveness of nose injection could be a smaller droplet concentration in the boundary layer along the side of the vehicle. Thus, even if the concentration of droplets in the stagnation region boundary layer was initially large, it would tend to decrease downstream of the hemisphere, since the outward momentum of the droplets would act so as to force them away from the vehicle surface as the flow expands around the hemisphere nose. Also, the high temperatures and densities in the boundary layer of the nose region would cause more rapid evaporation so that by the time the coolant reaches the downstream side regions, its concentration in the boundary layer would be further reduced. Under these conditions, the only mechanism that could cause any cooling effect would be a smaller local recovery temperature due to the reduction in free-stream stagnation temperature. Calculations by means of a simple droplet evaporation theory as applied to the inviscid stream indicate that the enthalpy potential for heat transfer to the wall can be reduced to at least one-half of its value without injection for conditions typical of the early part of the injection period. The evaporation theory used is described in the appendix. This effect of reducing the enthalpy potential would then reduce the heat input to the surface by the same factor, if there were no change in the boundary-layer flow itself.

Cyclic temperature variation caused by side injection.— Temperatures measured by thermocouples 1 to 5 on the beryllium nose as obtained directly from telemetered data points are plotted against time in figure 20. The switch sampling rate for these data was approximately 3 per second and every data point is shown during the time interval from 100 to 175 seconds. Although there is considerable scatter in the data, presumably due mostly to the sensitivity of the telemeter system, it can be seen that thermocouples 2, 4, and 5 (figs. 20(a), (b), and (c)), which are directly downstream of the side injection purses. The side and nose injection pulses are identified at the bottom of the figure. For thermocouple 2, these large decreases in temperature are evident through the fifth side injection pulse, up to 136 seconds. For thermocouples 4 and 5, the decreases occur only during the first four pulses of side injection, up to 130 seconds.

In contrast to the noted response to side injection of thermocouples 2, 4, and 5, thermocouples 1 and 3 (figs. 20(d) and (e)), which are displaced 90° laterally from the side injection ports, do not indicate any particular cooling effect during the side injection pulses. Rather, by comparison with the predicted temperature variation for no injection, there appears to be a gradual



increase in cooling effect starting at about 115 seconds. It should be noted that the predicted temperature variations shown in figure 20 are identical to those of figure 15, except that the curves have been adjusted downward to coincide with the data at 110 seconds. This adjustment was made so as to correct for heat conduction effects up to this time and also to afford a better comparison between computed and measured temperature variations.

It is thus apparent that side injection caused a large cooling effect, at least as far downstream as thermocouple 5, whereas nose injection caused a much smaller effect which was not evident until after 115 seconds. Possible reasons for the lack of large cooling effects after 136 seconds are considered in a subsequent section. The thermal response of the beryllium wall to the predicted heating rate for no injection is small as indicated by the corresponding predicted temperature variation at the inside and outside surfaces shown in figure 20(a). The effect of the thermal response time of the beryllium wall on temperatures at the inside surface with intermittent water injection is considered in the next section.

Thermal response of beryllium wall. The thermal response of the beryllium wall to a cyclic heat input variation was investigated theoretically by means of the computer program of reference 15. The assumed aerodynamic heat input to the exterior surface as used in this calculation is plotted against time in figure 21. The duration and timing of the negative heat pulses were chosen to match the first three side injection periods as indicated.

The inside and outside surface temperatures as obtained from this calculation are plotted against time in figure 22. It is evident that the inside surface temperature can be expected to follow this assumed cyclic heat input very closely. Moreover, the temperature-time slope at the inside surface adjusts rapidly to the changing inputs at the outside surface and is in close agreement with the slope at the outside surface. Consequently, the thin-skin-calorimeter technique of determining heating rates from measured temperature-time slopes at the inside surface is applicable in this case.

The telemetered data points from thermocouple 2 are shown for comparison in figure 22. The agreement in trends and temperature level between the data and the calculated values indicates that large negative heating rates occurred during side injection periods, and that these heating rates can be reliably estimated from the average temperature-time slope of the data points.

Quantitative analysis of the effect of water droplet evaporation and motion on boundary-layer profiles. A simplified method has been developed for predicting the effect of evaporation and motion of water droplets (or ice particles) on the boundary-layer profiles and surface heat transfer. A detailed description and derivation of the analysis and discussion of the assumptions is given in the appendix. The essential features are as follows:

The boundary layer that would normally exist just upstream of the liquid injection site is divided into a number of layers. Each layer is bounded by flow streamlines, and the water droplets initially deposited in a layer at the injection site are assumed to remain in that layer. The amount of water in





any particular layer is determined such that the ratio of mass flow rate of water to mass flow rate of air, W*, is constant across the boundary layer. The subsequent acceleration and evaporation of the water droplets in a layer is governed only by the mean gas velocity, density, and temperature in that layer. With the initial droplet diameter d₁ and mass-flow ratio W* as parameters, the effect of water addition on the momentum and enthalpy of the air-vapor mixture can then be determined at any downstream location. The values of W* used in the present analysis are based on values computed for inviscid stream conditions and typical injection rates as discussed in the appendix. Consistent with the simple evaporation theory used, shear forces, diffusion, and heat transfer between adjacent layers are neglected. The assumption is thereby made that the water droplet evaporation and motion are the predominant effects on the development and adjustment of the boundary layer just downstream of injection.

The initial boundary-layer profiles just upstream of the injection site were obtained with the computer program that was used for the real-gas, local-similarity, boundary-layer solutions of reference 14. The local conditions used for these profiles corresponding to the RAM B2 trajectory at 115 seconds and $\frac{x}{r_N} = 1.86$ on the sphere-cone were

$$H_e = 1.457 \times 10^8 \text{ ft}^2/\text{sec}^2$$
 $h_e = 0.911 \times 10^8 \text{ ft}^2/\text{sec}^2$
 $p_e = 0.0194 \text{ atm}$
 $T_e = 7160^\circ \text{ R}$
 $u_e = 1.045 \times 10^4 \text{ ft/sec}$
 $\beta = 0.244$
 $U' = 0.042$
 $h_w = 0.0437H_e$

For convenience these initial profiles were than divided into layers of uniform thickness in the transformed coordinate η (see ref. 14) of $\Delta \eta = 0.1$. The resulting step sizes Δy , in the physical plane, are shown on the left side of figure 23. Due to the large density near the wall, the values of Δy vary from about 0.25×10^{-3} foot at the surface to 0.85×10^{-3} foot at $y = 4.5 \times 10^{-3}$ foot. The total boundary-layer thickness for the conditions

used was approximately 0.058 foot; however, only the inner portion of the boundary layer out to $y = 4.5 \times 10^{-3}$ foot where $T \le 5000^{\circ}$ R is considered here so that ideal-gas relations can be used with reasonable accuracy. Also, in the simplified method used, only the temperature and thickness of the stream tube or layer next to the wall are required to estimate the wall heating rate.



Also shown in figure 23 is the variation in initial droplet diameter with distance out from the surface as computed from the correlation formula of reference 23. This formula is

$$d_{1} = 3.45 d_{0} \left(\frac{\sigma_{l}}{\rho_{a} u_{a}^{2} d_{o}} \frac{v_{l}}{u_{a} d_{o}} \right)^{1/4}$$
 (5)

which shows that for a given orifice diameter d_0 and liquid properties, the mean droplet diameter varies inversely as the product of the 1/4 power of the density and 3/4 power of the velocity. Thus, the droplet diameter computed from equation (5) is largest for the surface layer because of the small air velocity there. In fact, this droplet diameter for the surface layer is $d_1 = 7.75 \times 10^{-14}$ foot, which is larger than the thickness of the surface layer (2.5 \times 10⁻¹⁴ foot). Hence, it is believed that such large drop sizes are unrealistic, and due to factors such as migration of droplets between layers, a more realistic value is thought to be some average diameter for the region of the boundary layer shown in figure 23, such as $d_1 = 1.6 \times 10^{-14}$ foot, or approximately 50 microns.

The profiles at various downstream distances from the injection site were computed from the equations in the appendix for both the constant initial drop diameter of 50 microns and the variable drop diameters as shown in figure 23. The resulting profiles for the temperature and velocity of the air-vapor mixture are shown in figures 24 and 25 at distances from the injection site of 0.10, 0.39, 0.66, and 0.93 foot. The last three distances correspond approximately to the locations of thermocouples 2, 4, and 5. The initial boundary-layer profiles just upstream of the injection site (called s=0) are also shown in these figures. The symbol points in these figures are the midpoint location and conditions for each layer. In all cases only the inside portion of the boundary layer consisting of the original nine layers of figure 23 is shown. The temperature profiles for s>0 shown in figure 24(a) were computed for variable values of d_1 with $W^*=1.5$, whereas those in figures 24(b) and (c) are for $d_1=50$ microns for all layers and with $W^*=1.5$ and 3.0, respectively. The corresponding velocity profiles are shown in figures 25(a), (b), and (c), respectively.

Comparison of figures 24(a) and (b) shows that the use of the constant drop diameter results in a lower mixture temperature near the surface but a higher temperature farther out than does the variable drop diameter. This effect would be expected, since for a given water flow rate, more water is evaporated with small droplets than with large ones. A large value of W* (fig. 24(c)) results in lower temperatures in all layers and a larger increase in thickness of all layers. This effect of increasing the boundary-layer thickness is due primarily to the increased mass flow of gas as the water is evaporated.

Similar effects on the velocity profiles are evident in figure 25. That is, the use of the constant value of d_1 produces smaller velocities near the





surface and larger velocities farther out in the boundary layer than does the use of variable drop diameters. Thus, the smaller the initial droplet size, the more the gas mixture velocity is reduced. The reason for this apparent paradoxical behavior is that the small droplets can be accelerated faster, thereby removing momentum from the gas stream at a greater rate. Figure 25(c) shows that the velocities are reduced in all layers when W* is increased.

The quantity R^3 is the cube of the ratio of the local droplet diameter to the initial value and is thus equal to the fraction of the injected water still in liquid form. In order to illustrate the different evaporation rates resulting from the various initial droplet diameters and values of W^* used in figures 2^{14} and 2^{5} , the values of R^3 are plotted against distance from the wall in figure 2^{6} for the same three sets of conditions used in the former figures. Comparison of figures 2^{6} (a) and (b) shows that more of the liquid is evaporated when the drops are small. Comparison of figures 2^{6} (b) and (c) shows that less of the injected liquid is evaporated for $W^* = 3.0$ than for $W^* = 1.5$. However, relatively more water is actually evaporated in the former case since the mass ratio of water vapor flow rate to airflow rate is given by

$$\frac{\dot{\mathbf{m}}_{\mathbf{v}}}{\dot{\mathbf{m}}_{\mathbf{a}}} = \mathbf{W}^* \left(1 - \mathbf{R}^3 \right) \tag{6}$$

Effect of water droplet evaporation on heat-transfer rate to vehicle surface. The experimental heating rates during side injection pulses have been estimated at thermocouple positions 2, 4, and 5 by using equation (3) with the corresponding temperature-time slopes obtained directly from the data of figures 20(a), (b), and (c). The resulting heating rates for the first five side injection pulses are plotted against distance from the injection site in figure 27. These heat-transfer rates are generally negative (indicating heat was removed from the surface) and tend to become less negative at greater distances from the injection site and at later times corresponding to higher altitudes.

For comparison with these experimental data, the droplet evaporation theory described in the previous section has been used to calculate the surface heat-transfer rates during the side injection pulses. This calculation was done by assuming a linear temperature variation between the computed temperatures in the layer next to the wall and the surface temperature which, for the 115-second case, had a value of approximately 10600 R. Thus, the theoretical heat-transfer rate to the surface is given by the expression

$$q_{w} = k_{m,w} \left(\frac{T_{m} - T_{w}}{\frac{\Delta y}{2}} \right)_{sl}$$
 (7)

where the subscript sl indicates that T_m and Δy are evaluated for the layer next to the surface. The thermal conductivity of the gas mixture evaluated at the wall, $k_{m,\,w}$, was assumed to be the same as that of air at the wall temperature. This assumption seems reasonable for two reasons. First, the actual mole fraction of water vapor present in the layer next to the wall is



small. The mole fraction of water vapor to air is obtained from equation (6) multiplied by the ratio of the molecular weight of air to the molecular weight of water, and is thus

$$\left(\frac{28.97}{18.02}\right)$$
W* $\left(1 - R^{3}\right)$

The values of \mathbb{R}^3 from figure 26 are $\mathbb{R}^3 \geq 0.93$ in the wall layer for x = 0.39 where the large changes in wall heating are already encountered. For $\mathbb{W}^* = 1.5$, the resulting mole fraction ratio of water vapor to air is ≤ 0.17 . Second, the thermal conductivity for pure steam is about 0.9 of that for air at these temperatures (see refs. 24 and 25) so that even for mole fractions much closer to unity, the thermal conductivity of the mixture would be close to that of air.

The results of the calculation are plotted in figure 27. Each curve is labeled with the values of W*, d₁, and trajectory time used to determine input conditions. Consider first the four curves for 115 seconds. With W* = 1.5 and d₁ varied according to figure 23 (d₁, w ≈ 240 microns) the predicted cooling rates are considerably smaller (less negative) than the experimental values at 115 seconds. When d₁ = 50 microns, the predicted values are in good agreement with the data at the first two thermocouple positions, and about the same results are obtained with both W* = 1.5 and W* = 3.0. When the drop diameter is assumed to be 5 microns, the predicted cooling rates are considerably too large. From these results it can be concluded that the value of W* used in the theory is less critical than the initial drop diameter and a value of d₁ = 50 microns is about right. Note that this value of d₁ is based on the correlations of reference 23 (eq. (5)) applied at some small distance away from the wall. In this case, this distance was 2 × 10⁻³ foot or about 3.5 percent of the initial boundary-layer thickness.

As was noted previously, the experimental data indicate that for later times corresponding to higher altitudes the cooling effect of water injection becomes smaller and tends to approach zero at thermocouple 5. In order to further check the theoretical method used, two cases were computed for conditions at 135 seconds with $W^* = 3.0$ and values of d_1 of 67 and 5 microns. The former value of d_1 was obtained from equation (5) applied at a point about 3.5 percent of the total boundary-layer thickness from the wall as in the 115-second case. The results for $d_1 = 67$ microns are again in good agreement with the data, but only at the first thermocouple station. The predicted cooling rates for $d_1 = 5$ microns are too large. Apparently, the theoretical prediction method is still valid at 135 seconds when the mean value of d_1 as obtained with the correlation of reference 23 is used. The reduction in cooling effectiveness at the higher altitudes is apparently caused by the smaller evaporation rate, which in turn is due to the reduced densities.

The discrepancy between predicted and measured heating rates at the downstream stations for both 115 and 135 seconds is probably caused partly by the





assumption of negligible heat conduction and shear between layers in the simple flow model used. This assumption would not be expected to apply except just downstream of the injection site. Another factor that may be partly responsible for the observed discrepancy would be a tendency for a reduction in droplet concentration at the downstream stations. That is, the droplets probably have slight outward, as well as lateral, velocity components both of which would result in smaller coolant concentrations in the downstream regions as compared with the theoretical predictions for which W* is assumed constant. Another possible mechanism that could contribute to the observed cooling effect is separation due to the liquid jets. This mechanism could become more important at higher altitudes; however, no attempt was made to include separation effects in the present analysis. Data of reference 13 indicate that separation effects would generally be small except for large relative injection rates and small Reynolds numbers.

Also included in figure 27 are theoretical heating rates for no injection computed as described previously from figures 11 and 13. Comparison of these values at s=0 with the values computed directly ($q_{\rm w}=13.8~{\rm Btu/ft^2-sec}$ and $q_{\rm w}=9.6~{\rm Btu/ft^2-sec}$ at 115 and 135 seconds, respectively) from the similar boundary-layer solution used in the evaporation theory indicates that the latter values are lower by about 25 and 20 percent at 115 and 135 seconds, respectively. These differences are apparently caused by slight discrepancies in input conditions for the calculations and other differences in the methods such as the correlations used in the calculations of figures 11 and 13.

CONCLUSIONS

Temperature measurements obtained on the beryllium nose cone and the ablation-protected aluminum substructure of a spherically blunted cone-cylinder model (RAM B2) during ascent flight have been analyzed and compared with theoretical predictions. The effect of intermittent water injection on surface heat transfer has been determined and also compared with theoretical predictions. The following conclusions have been made:

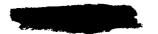
- 1. The boundary layer on the beryllium cone was turbulent up to an altitude of about 65 000 feet and a flight velocity of 4000 ft/sec. The indicated heat-transfer rates during this period were compared with predictions from a local flat plate theory and an integral theory for turbulent boundary layers. The data were generally in better agreement with the latter theory, but were still below the predicted values by 20 to 30 percent.
- 2. Transition from turbulent to laminar boundary layer occurred for local Reynolds numbers (based on flow length) from 1 \times 10⁶ to 1.5 \times 10⁶ and local Mach numbers of about 2.2. The minimum critical Reynolds number for transition at these conditions and for this body shape was therefore approximately 1 \times 10⁶.
- 3. The properties of the ablation material used in a numerical calculation for the temperatures of the supporting substructure resulted in good agreement



with measured temperatures except at the most forward station. The response time to the initial heat pulse at this forward station was too small to be consistent with the initial material thickness. A possible explanation is that some loss of material occurred because of large shear and pressure loads in the first 10 to 20 seconds of the flight.

- 4. Water injection from side ports, which were located just downstream of the sphere-cone junction, resulted in a much larger cooling effect than injection from the stagnation region. The first four or five pulses of side injection caused a marked reduction in temperature of the beryllium wall at the instrumented stations, which were all within 1 foot downstream of the injection site.
- 5. A theoretical method for predicting the magnitude of the cooling effect of side injection was derived and found to be in agreement with the data, as far downstream as 0.7 foot from the injection site, provided that initial water droplet diameters were based on correlations of NACA TN 4087. At a distance of 1 foot from the injection site, the theory overpredicted the cooling effect, presumably due to the simplifying assumptions used.

Langley Research Center,
National Aeronautics and Space Administration,
Langley Station, Hampton, Va., March 23, 1965.



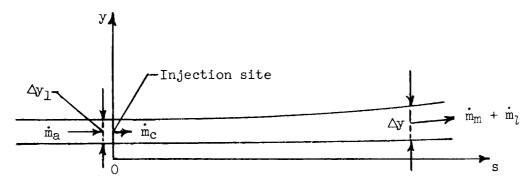


ANALYSIS OF DROPLET MOTION AND EVAPORATION IN A BOUNDARY LAYER

One-Dimensional Theory for Droplet Motion and Evaporation

The following theoretical analysis is intended to provide first-order estimates of spray evaporation times and distances. The analysis is similar to the drop evaporation theory of reference 1 except that the air and water vapor are treated as ideal gases with constant specific heats and no dissociation. Application of the present analysis is thereby limited to the inner portion of the boundary layer where temperatures are less than about 5000° R.

Steady flow is assumed and the conservation of mass, momentum, and energy is required in a control volume consisting of a two-dimensional stream tube as indicated in the following sketch:



The droplets are assumed to be deposited in the stream tube at s = 0 with a small s component of velocity. The y velocity components of both the droplets and air-vapor mixture are neglected. The assumption of a small streamwise or s component of droplet velocity is consistent with the installation of the RAM B2 side injection orifices, which were normal to the vehicle surface. The assumption of a small or negligible normal or cross-current droplet velocity component is perhaps not as obvious. However, if any droplets at all are deposited in the boundary layer close to the surface they would of necessity have small y velocity components. Although the mean velocity of the liquid jet is not negligible and is certainly normal to the surface, the liquid velocity at the extreme edges of the jet would be very small. It is thought that the droplets in the boundary layer originate from these edge regions of the jet.

Conservations of mass.- If no droplets cross the stream-tube boundaries, then

$$\dot{\mathbf{m}}_{a} + \dot{\mathbf{m}}_{c} = \dot{\mathbf{m}}_{m} + \dot{\mathbf{m}}_{l} \tag{Al}$$





where, per unit width of stream tube,

$$\dot{\mathbf{m}}_{\mathbf{a}} = \left(\rho_{\mathbf{a}} \mathbf{u}_{\mathbf{a}} \, \Delta \mathbf{y} \right)_{\mathbf{1}} \tag{A2}$$

The area occupied by the gas mixture of air and evaporated liquid at any station is

$$A_{\mathbf{m}} = \frac{\dot{\mathbf{m}}_{\mathbf{m}}}{\rho_{\mathbf{m}} \mathbf{u}_{\mathbf{m}}} \tag{A3}$$

and the area occupied by the liquid (or frozen) droplets is

$$A_{l} = \frac{\dot{m}_{l}}{\rho_{l} u_{d}} \tag{A4}$$

Hence, the total stream-tube area at any station, per unit width, is from equations (A3) and (A4)

$$\Delta y = \frac{\dot{m}_{m}}{\rho_{m}u_{m}} + \frac{\dot{m}_{l}}{\rho_{l}u_{d}} \tag{A5}$$

If it is assumed that the droplets are all initially of the same size and evaporate at the same rate, then

$$\frac{\dot{m}_1}{\dot{m}_c} = \left(\frac{d}{d_1}\right)^3 = R^3 \tag{A6}$$

so that with the definition $W^* = \frac{\dot{m}_c}{\dot{m}_c}$,

$$\dot{\mathbf{m}}_{7} = \mathbf{W}^{*} \mathbf{R}^{3} \dot{\mathbf{m}}_{\mathbf{a}} \tag{A7}$$

Then, from equations (Al) and (A7) an expression for the mass flow of the gas mixture is obtained as

$$\dot{\mathbf{m}}_{\mathbf{m}} = \dot{\mathbf{m}}_{\mathbf{a}} \left[1 + \mathbf{W}^* \left(1 - \mathbf{R}^3 \right) \right] \tag{A8}$$

Substitution of equations (A7) and (A8) into equation (A5) and the use of equation (A2) for \dot{m}_a gives the final expression for the change in stream-tube area as

$$\frac{\Delta y}{\Delta y_1} = \frac{(\rho_a u_a)_1}{\rho_m u_m} \left[1 + W^* \left(1 - R^3 \right) \right] + \frac{(\rho_a u_a)_1}{\rho_1 u_d} R^3 W^*$$
(A9)





Conservation of momentum.— The mixing and evaporation process is assumed to occur at constant pressure. The assumption of constant pressure is based on the data of reference 13 where liquid was injected from a single orifice on a sphere-cone model. These data showed that the effect of injection on model static pressures was small for injection rates comparable to the smaller values of W^* used herein. Hence, by neglecting shear forces at the stream-tube boundaries, the momentum equation can be written as

$$\dot{m}_{a}u_{a,1} + \dot{m}_{c}u_{d,1} = \dot{m}_{m}u_{m} + \dot{m}_{l}u_{d}$$
 (A10)

By solving this equation for u_m and using equations (A7) and (A8), there is obtained

$$u_{m} = \frac{u_{a,1} + w^{*}u_{d,1} - w^{*}R^{3}u_{d}}{1 + w^{*}(1 - R^{3})}$$
(A11)

Conservation of energy. By neglecting heat transfer at the stream-tube boundaries, the energy equation is written as

$$\dot{m}_{a}\left(h_{a} + \frac{u_{a}^{2}}{2}\right)_{1} + \dot{m}_{c}\left(h_{l,1} + \frac{u_{d,1}^{2}}{2}\right) = \dot{m}_{m}\left(h_{m} + \frac{u_{m}^{2}}{2}\right) + \dot{m}_{l}\left(h_{l} + \frac{u_{d}^{2}}{2}\right) \tag{A12}$$

The latent heat of the liquid is given by the expression

$$L = (h_v - h_l)_{sat}$$

Then, with the assumption that

$$h_l = h_{l,1} = h_{l,sat}$$

and with the use of equations (A7) and (A8), equation (A12) can be written in the form

$$c_{p,m}T_{m} = \frac{\left(h_{a} + \frac{u_{a}^{2}}{2}\right)_{1} - w^{*}(1 - R^{3})(L - h_{v,sat}) + w^{*}\left(\frac{u_{d,1}^{2}}{2} - R^{3}\frac{u_{d}^{2}}{2}\right)}{1 + w^{*}(1 - R^{3})} - \frac{u_{m}^{2}}{2}$$
(A13)

Motion of droplets.- The drag force on each droplet is

$$F = \frac{1}{2} \pi r^2 \rho_m V^2 C_D \tag{A14}$$

where V is the relative velocity between the gas mixture velocity and the droplet velocity; that is,

$$V = u_m - u_d$$



The instantaneous acceleration of the droplets is then given by

$$\frac{\mathrm{du}_{\mathrm{d}}}{\mathrm{dt}} = \frac{3}{8} \frac{\rho_{\mathrm{m}} V^{2} C_{\mathrm{D}}}{\rho_{l} r_{1} R} \tag{A15}$$

where it has been assumed that the evaporating molecules leave the droplet surface uniformly on all sides and thus contribute no net force.

For convenience in machine computations, two expressions for drag coefficient for different ranges in Mach number are used. For $M_{\rm d} \ge 0.5$ an expression similar to that of reference 26 is

$$C_{D} = C_{D,C} + (C_{D,FM} - C_{D,C})e^{-A(N_{R,d})^{n}}$$
 (A16)

where

$$M_{\rm d} = \frac{V}{\sqrt{\gamma_{\rm m} \overline{R}_{\rm m} T_{\rm m}}} \tag{A17}$$

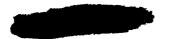
$$N_{R,d} = \frac{\rho_m V d}{\mu_f}$$
 (A18)

The quantities $C_{\mathrm{D,C}}$, $C_{\mathrm{D,FM}}$, A, and n are given as functions of $\mathrm{M_d}$ in reference 1. The basic expression of reference 26 was modified to match the data of references 27 to 29. The values for the continuum drag coefficient $C_{\mathrm{D,C}}$ are taken from the data of references 30 and 31. The values for the free-molecule drag coefficient $C_{\mathrm{D,FM}}$ are taken from reference 32 (p. 704). An expression for $\mathrm{M_d} < 0.5$ was also derived to match available data (refs. 33 and 34) and is

$$C_{D} = \frac{\overline{C}_{D} + \frac{51.1M_{d}}{N_{R,d}}}{1 + 0.256M_{d}\left(\overline{C}_{D} + \frac{51.1M_{d}}{N_{R,d}}\right)}$$
(A19)

where

$$\overline{c}_{D} = \frac{24}{N_{R,d}} + 0.4 + 1.6e^{-0.028(N_{R,d})^{0.82}}$$
 (A20)





Heat transfer to droplets. The heat-transfer rate per unit area q into a drop is assumed to be used entirely for the heat of vaporization so that

$$4\pi r^2 q = -\frac{4}{3}\pi \rho_l L \frac{dr^3}{dt}$$

or

$$q = -\frac{1}{2} \frac{\rho_l L}{r} \frac{dr^2}{dt}$$
 (A21)

The Nusselt number for heat transfer to the droplets is defined as

$$N_{Nu} = \frac{qdc_{p,v}}{k_f \left[f_{r,0} \frac{v^2}{2} + c_{p,m} \left(T_m - T_d\right)\right]}$$
(A22)

The droplet evaporation rate from equations (A21) and (A22) is thus

$$\frac{dR^{2}}{dt} = -\frac{k_{f}N_{Nu}}{\rho_{l}Lr_{l}^{2}c_{p,v}} \left[f_{r,0} \frac{v^{2}}{2} + c_{p,m} (T_{m} - T_{d}) \right]$$
(A23)

Equation (A23) leads to the well-known result that the square of the droplet diameter varies as a linear function of time for evaporation of an isolated droplet in a low-velocity gas stream where N_{Nu} is approximately constant.

In the present situation, the local stream properties may vary significantly as the droplets evaporate, and the Nusselt number may vary from values in the free-molecule regime to values in the continuum regime. In order to provide for a continuous transition from free-molecule to continuum values and also to include the effect of mass transfer on heat transfer, the Nusselt number is written as

$$N_{Nu} = \frac{N_{Nu,C}(q/q_0)}{1 + \frac{N_{Nu,C}(q/q_0)}{N_{Nu,FM}}}$$
(A24)

which is similar to an expression given in reference 35. The quantity q/q_0 is the ratio of the heat transfer with mass transfer to the corresponding value for no mass transfer and is evaluated from reference 36 (p. 21) as

$$\frac{q}{q_0} = \frac{L}{c_{p,v} \Delta T} \ln \left(1 + \frac{c_{p,v} \Delta T}{L} \right)$$
 (A25)





where

$$\Delta T = f_{r,0} \frac{V^2}{2c_{p,m}} + T_m - T_d$$

The expression for the Nusselt number in continuum flow is (ref. 36, p. 22)

$$N_{Nu,C} = 2 + 0.6(N_{Pr,f})^{1/3}(N_{R,d})^{1/2}$$
 (A26)

where

$$N_{Pr,f} = \left(\frac{c_p \mu}{k}\right)_f$$

The Nusselt number for free-molecule flow is written as

$$N_{Nu,FM} = \frac{\gamma_{m} + 1}{\gamma_{m}} N_{St,FM} \rho_{m} VR d_{1} \frac{c_{p,v}}{k_{f}} \frac{f_{r}}{f_{r,0}} \frac{\frac{v^{2}}{2} + c_{p,m} (T_{m} - T_{d})}{\frac{v^{2}}{2} + c_{p,m} (T_{m} - T_{d})}$$
(A27)

The free-molecule Stanton number $N_{\text{St,FM}}$ is given in reference 32 (p. 699) and can be matched satisfactorily by the expression

$$N_{St,FM} = \frac{0.104}{S^{1.14}} + 0.125 \left(1 - e^{-1.17S^{0.408}}\right)$$
 (A28)

where

$$S = \frac{V}{\sqrt{2\overline{R}_{m}T_{m}}}$$

The free-molecule recovery factor f_r (ref. 32, p. 699) can be matched by the expression

$$f_r = \frac{\gamma_m}{\gamma_m + 1} (2 + 0.7e^{0.707S})$$
 (A29)

Thermodynamic properties of gas mixture. The thermodynamic properties of the mixture of air and water vapor depend on the ratio of the mass of evaporated water to the mass of air, which is

$$\overline{W} = W^*(1 - R^3)$$





The ideal-gas law is used for the density

$$\rho_{\rm m} = \frac{p}{\overline{R}_{\rm m} T_{\rm m}} \tag{A30}$$

where

$$T_{m} = \frac{1 + \overline{W}}{c_{p,a} + \overline{W}c_{p,v}} h_{m}$$
 (A31)

$$\overline{R}_{m} = \frac{\overline{R}_{a} + \overline{W}\overline{R}_{v}}{1 + \overline{W}}$$
 (A32)

The ratio of specific heats is

$$\gamma_{\rm m} = \left(1 + \frac{\overline{R}_{\rm a} + \overline{W}\overline{R}_{\rm v}}{c_{\rm p, a} + \overline{W}c_{\rm p, v}}\right)^{-1} \tag{A33}$$

Transport properties of film. The film transport properties as used in equations (Al8), (A22), and (A26) are evaluated at the film temperature defined as

$$T_{f} = \frac{1}{2} \left(\frac{v^{2}}{2c_{p,m}} + T_{m} + T_{d} \right)$$
 (A34)

The film viscosity was computed from the mixture formula of reference 37 (constants for the viscosities of air and water vapor were taken from ref. 38) with mole fractions of air and water vapor modified to represent an average composition in the film. Thus, the mole fraction of the water vapor in the film is

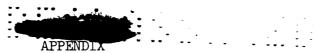
$$X_{v,f} = \frac{1}{2} (X_{v,d} + X_{v,m})$$
 (A35)

where $X_{V,d}$ is the mole fraction of vapor at the drop surface, usually taken as one. The mole fraction of air in the film is then

$$X_{a,f} = \frac{1 - X_{v,f}}{1 - X_{v,m}} X_{a,m}$$
 (A36)

so that $X_{v,f} + X_{a,f} = X_{v,m} + X_{a,m} = 1$





Two alternate methods for the calculation of film thermal conductivity were used. In method 1, the term which would normally appear in the mixture equation of reference 37 for water vapor as

$$0.88 \left(\frac{2}{5} \frac{c_{p,v}}{\overline{R}_{v}} - 1\right)$$

was replaced by

$$\frac{4}{15} \frac{c_{p,v}}{\overline{R}_v} - 1$$

since on the basis of data for water vapor in references 24 and 39 the value of the Prandtl number for water vapor may be assumed unity for a wide range of conditions. In method 2, the film viscosity was assumed to be just that of water vapor calculated by using the method and constants of reference 38. The film thermal conductivity was then computed from this viscosity by assuming $P_{r,f} = 1$ and using the specific heat of water vapor as $11.580 \text{ ft}^2/\text{sec}^2$. The specific heat of air was taken as $5997 \text{ ft}^2/\text{sec}^2$. Method 2 was used for the results given in this report; however, method 1 gave substantially the same results.

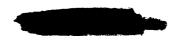
The equations derived in this appendix have been programed for solution on a high-speed electronic data processing machine. The techniques used in the solution are the same as those of reference 1.

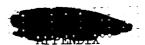
Application of Evaporation Theory to Boundary-Layer Flow

Basic assumptions.— It is assumed that for some short distance downstream of the injection site, the predominant effects on flow changes are caused by the evaporation and acceleration of the droplets. The simplified droplet evaporation and motion theory just described is thereby applied directly to stream tubes in an established laminar boundary layer. The choice of stream-tube dimensions is somewhat arbitrary; however, the height of the stream tubes should be as small as practical, consistent with the droplet size used and the accuracy of the initial boundary-layer profiles. The method for determining Δy_1 in the present calculation is discussed in the text of this report.

Another assumption used is that the droplets in any particular stream tube are all of the same size initially and evaporate at the same rate, so one droplet size and the initial mean flow conditions characterize the situation for that stream tube. In order to obtain a finite initial value for the ratio $\Delta y/\Delta y_1$ from equation (A9), it is necessary to specify a finite value for $u_{\rm d,1}.$ In the present application these values were chosen such that

$$\frac{\left(\rho_{\mathbf{a}}\mathbf{u}_{\mathbf{a}}\right)_{1}}{\rho_{l}\mathbf{u}_{\mathbf{d},1}} = 0.001$$





In the portion of the boundary layer considered, the resulting values of $u_{d,1}$ were less than 6 ft/sec, which seems consistent with the cross-current injection configuration used for the side sites on RAM B2. (See fig. 2.)

Determination of values for W*.- The actual distribution of coolant across the boundary layer is unknown; however, a reasonable assumption for this distribution is obtained as follows: The small physical thickness of the boundary layer (less than 1 inch for the RAM B2 case) and the likelihood that the amount of water eroded from a liquid jet as it passes through the boundary layer depends mainly on the local air mass flow suggest that W* may be constant across the boundary layer. Observations of water spray distribution reported in reference 13 generally indicated a uniform concentration of droplets in the portion of the flow field near the body. The droplet concentration per unit width in a given stream tube is

$$N_{d} = \frac{\dot{m}_{c}}{\frac{1}{3} \pi r_{1}^{3} \rho_{l} u_{d} \Delta y}$$

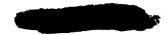
With the definition of W*, this equation may be written as

$$N_{d} = \frac{W^{*}}{\frac{1}{3}\pi r_{1}^{3}} \frac{\left(\rho_{a} u_{a} \Delta y\right)_{1}}{\rho_{l} u_{d} \Delta y}$$
(A37)

Thus, if the last factor on the right were constant, then (for r_1 constant) the assumption of constant W^* would be consistent with a constant droplet concentration. In order to check this possibility, the factor $\frac{\rho_l u_d}{\left(\rho_a u_a \ \Delta y\right)_l}$

(as obtained from the numerical solutions with W^* constant) is plotted in figure 28 against y at values of s of 0.1 and 0.39 foot for the conditions of figure 24(c) (W^* = 3.0; d_1 = 50 microns, constant). At s = 0.1 foot, where the present theory should apply with the best accuracy, the variation in this factor is small. At s = 0.39 foot, the variation in the factor is larger and would indicate a smaller concentration of droplets near the surface. In view of the other approximations and assumptions made in the theory, this variation in the droplet concentration factor is not considered large enough to invalidate the assumption of constant W^* . If anything, the value of W^* should probably be somewhat larger near the wall than in the inviscid stream, in order to keep N_d constant.

The values of w^* in the inviscid stream depend on the maximum cross-current penetration of the spray and its lateral distribution. The maximum cross-current penetration of the spray, y'_{max} , for the RAM B2 body shape is obtained from the correlations of reference 13. For water injection the formula for y'_{max} is (ref. 13)





$$\frac{y_{\text{max}}'}{d_0} = 1.79 \left[\frac{\rho_l u_l}{\rho_\infty u_\infty} \left(\frac{p_a}{p_v} \right)^{-0.24} \right]^{0.25} \left(\frac{x'}{d_0} \right)^{0.5}$$
(A38)

where u_l is the liquid velocity at the exit of the injection orifice and p_a/p_v is the ratio of the ambient or air static pressure to the liquid vapor pressure at the injection site. By the application of equation (A38) to RAM B2 trajectory conditions at times of 120 and 170 seconds and with the use of figure 10 for the injection velocity u_l , the results shown in figure 29 were obtained. The value of y_{max}^l from the calculation is the normal distance from an x'-coordinate axis which is alined with the free-stream flow direction and passes through the injection orifice. The distance from the surface, as shown in figure 29, is thus

$$\Delta y_{\text{max}}^{\dagger} = y_{\text{max}}^{\dagger} - x^{\dagger} \tan 9^{\circ}$$

Also included in the figure is the distance from the surface to the shock wave as obtained from reference 40.

Comparison of the maximum spray penetration with the shock location as shown in figure 29 indicates that for most of the injection period, the spray penetration is slightly less than or somewhat greater than the shock layer thickness. A reasonable estimate of W^{X} that would represent a mean value in the region of the spray would then be given by

$$W^* = \frac{\frac{1}{2}(\dot{m}_c)_{\text{total}}}{\pi(R_b + \Delta y_{\text{max}})^2 \rho_{\infty} u_{\infty} f_s}$$
(A39)

where R_b is the body radius, Δy_{max} is the maximum spray penetration from the body surface, f_s is the fraction of the total 360° around the body that is occupied by the spray from one side, and $(\dot{m}_c)_{total}$ is the total mass flow for side injection as obtained from figure 9. Maximum and minimum values of $\frac{1}{2}(\dot{m}_c)_{total}$ from figure 9 are listed in the following table:

Time, sec	$\left(\dot{\mathtt{m}}_{\mathtt{C}}\right)_{\mathtt{min}}$ per side, lb/sec	$\left(\dot{\mathtt{m}}_{\mathtt{c}} ight)_{\mathtt{max}}$ per side, lb/sec
115	0.10	0.60
135	.06	.37
165	.04	.15

The corresponding values of W^* computed from equation (A39) for thermocouple 2 are plotted against time in figure 30. The assumed values of f_s are also

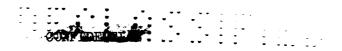




shown in this figure and are based on observations in reference 13 that the spray, even from a single orifice, may spread at least halfway around the body when $p_{\rm V}/p_{\rm a}$ is large, corresponding, in this case, to the higher altitudes. From the results shown in figure 30, and the preceding discussion, it is believed that the values of W* of 1.5 and 3.0 are realistic for applying the theory to the RAM B2 conditions and correspond to the maximum flow rates used.

Results.- The values of ρ_m , u_m , u_d , R, and T_m for each layer were obtained as functions of s from the numerical solution of the droplet evaporation equations given previously. The use of these values in equation (A9) gives the local stream-tube thickness which is then summed across the boundary layer to determine the distance from the wall to the midpoint of each stream tube. Plots of T_m , u_m , and R^3 against this distance from the wall are given in figures 24, 25, and 26 for various values of s, which is the streamwise distance from the injection site.

The heat-transfer rate to the vehicle surface is obtained by assuming a linear temperature distribution between the midpoint of the layer next to the surface and the wall temperature that prevails just before the start of a side injection pulse. This wall temperature would be the value at the surface for s=0 as shown, for example, in figure 24. The assumption of a linear temperature distribution next to the surface is believed to be reasonable for small distances (say s<0.4 ft) downstream from injection and small times (say 1 second) from the initiation of an injection pulse.



REFERENCES

- 1. Cuddihy, W. F.; Beckwith, I. E.; and Schroeder, L. C.: A Solution to the Problem of Communications Blackout of Hypersonic Reentry Vehicles. AMRAC Proceedings, Vol. IX, Pt. II, Inst. Sci. Technol., Univ. of Michigan, 1963, pp. 187-231. (Available from DDC as AD 344 601 (4613-59-X, pt. II).)
- 2. Cuddihy, William F.; Beckwith, Ivan E.; and Schroeder, Lyle C.: RAM B2 Flight Test of a Method for Reducing Radio Attenuation During Hypersonic Reentry. NASA TM X-902, 1963.
- 3. Cuddihy, William F.: Results of the RAM B2 Materials-Addition Flight Experiment. Proceedings of the NASA Conference on Communicating Through Plasmas of Atmospheric Entry and Rocket Exhaust, NASA SP 52, 1964, pp. 203-211.
- 4. Raper, James L.; Keynton, Robert J.; and Woodbury, Gerard E.: Detailed Description and Flight Performance of the RAM B Vehicle. NASA TN D-2437, 1964.
- 5. Carter, Howard S.; and Wright, Robert L.: Heat Transfer to a Hemispherically Blunted 9° Half-Angle Cone During Free Flight at Mach Numbers up to 20.8. NASA TM X-908, 1963.
- 6. Wright, Robert L.; and Carter, Howard S.: Heat Transfer to a Hemispherically Blunted 9° Half-Angle Cone-Cylinder at Hypersonic Free-Flight Mach Numbers up to 20.4. NASA TM X-1009, 1964.
- 7. Herrick, John: Avcoat External Thermal Insulation Development Program. RAD-SR-61-87 (Contract AF04(647)-258), Res. and Advanced Develop. Div., AVCO Corp., June 9, 1961.
- 8. Stalder, Jackson R.: The Useful Heat Capacity of Several Materials for Ballistic Nose-Cone Construction. NACA TN 4141, 1957.
- 9. Storer, E. M.: Summary of Flow Field Pressure Distributions on Sphere Cones at Several Mach Numbers and Altitudes. Aerodyn. Data Memo No. 2:23, Missile and Space Vehicle Dept., Gen. Elec. Co., Dec. 1961.
- 10. Gravalos, F. G.; Edelfelt, I. H.; and Emmons, H. W.: The Supersonic Flow About a Blunt Body of Revolution for Gases at Chemical Equilibrium. Tech. Inf. Series No. R58SD245 (Contract AF 04(645)24), Missile and Ord. Syst. Dept., Gen. Elec. Co., June 16, 1958.
- 11. Huber, Paul W.: Hypersonic Shock-Heated Flow Parameters for Velocities to 46,000 Feet Per Second and Altitudes to 323,000 Feet. NASA TR R-163, 1963.
- 12. Moeckel, W. E.; and Weston, Kenneth C.: Composition and Thermodynamic Properties of Air in Chemical Equilibrium. NACA TN 4265, 1958.



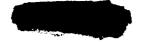


- 13. Beckwith, Ivan E.; and Huffman, Jarrett K.: Injection and Distribution of Liquids in the Flow Fields of Blunt Shapes at Hypersonic Speeds. NASA TM X-989, 1964.
- 14. Cohen, Nathaniel B.: Boundary-Layer Similar Solutions and Correlation Equations for Laminar Heat-Transfer Distribution in Equilibrium Air at Velocities up to 41,100 Feet Per Second. NASA TR R-118, 1961.
- 15. Swann, Robert T.; and Pittman, Claud M.: Numerical Analysis of the Transient Response of Advanced Thermal Protection Systems for Atmospheric Entry. NASA TN D-1370, 1962.
- 16. Lees, Lester: Laminar Heat Transfer Over Blunt-Nosed Bodies at Hypersonic Flight Speeds. Jet Propulsion, vol. 26, no. 4, Apr. 1956, pp. 259-269, 274.
- 17. Beckwith, Ivan E.; and Cohen, Nathaniel B.: Application of Similar Solutions to Calculation of Laminar Heat Transfer on Bodies With Yaw and Large Pressure Gradient in High-Speed Flow. NASA TN D-625, 1961.
- 18. Falkner, V. M.: A New Law for Calculating Drag The Resistance of a Smooth Flat Plate With Turbulent Boundary Layer. Aircraft Engineering, vol. XV, no. 169, Mar. 1943, pp. 65-69.
- 19. Beckwith, Ivan E.; and Gallagher, James J.: Heat Transfer and Recovery Temperatures on a Sphere With Laminar, Transitional, and Turbulent Boundary Layers at Mach Numbers of 2.00 and 4.15. NACA TN 4125, 1957.
- 20. English, Roland D.; and Carter, Howard S.: Variation in Heat Transfer During Transient Heating of a Hemisphere at a Mach Number of 2. NASA TN D-399, 1960.
- 21. Deveikis, William D.; and Walker, Robert W.: Local Aerodynamic Heat Transfer and Boundary-Layer Transition on Roughened Sphere-Ellipsoid Bodies at Mach Number 3.0. NASA TN D-907, 1961.
- 22. Cohen, Nathaniel B.: A Method for Computing Turbulent Heat Transfer in the Presence of a Streamwise Pressure Gradient for Bodies in High-Speed Flow. NASA MEMO 1-2-59L, 1959.
- 23. Ingebo, Robert D.; and Foster, Hampton H.: Drop-Size Distribution for Crosscurrent Breakup of Liquid Jets in Airstreams. NACA TN 4087, 1957.
- 24. Fano, Lilla; Hubbell, John H.; and Beckett, Charles W.: Compressibility Factor, Density, Specific Heat, Enthalpy, Entropy, Free-Energy Function, Viscosity, and Thermal Conductivity of Steam. NACA TN 3273, 1956.
- 25. Hilsenrath, Joseph; Beckett, Charles W.; et al.: Tables of Thermal Properties of Gases. NBS Circ. 564, U.S. Dept. Comm., 1955.





- 26. Masson, David J.; Morris, Deane N.; and Bloxsom, Daniel E.: Measurements of Sphere Drag From Hypersonic Continuum to Free-Molecule Flow. Rarefied Gas Dynamics, L. Talbot, ed., Academic Press, Inc. (New York), 1961, pp. 643-661.
- 27. Aroesty, Jerome: Sphere Drag in Low Density Supersonic Flow. Rept. No. HE-150-192 (Contract N-onr-222(45)), Inst. Eng. Res., Univ. of California, Jan. 3, 1962.
- 28. Sreekanth, A. K.: Drag Measurements on Circular Cylinders and Spheres in The Transition Regime at a Mach Number of 2. Rept. No. 74, Inst. Aerophys., Univ. of Toronto, Apr. 1961.
- 29. Ashkenas, Harry: Low-Density Sphere Drag With Equilibrium and Nonequilibrium Wall Temperature. Rarefied Gas Dynamics, Vol. II, J. A. Laurmann, ed., Academic Press, 1963, pp. 278-290.
- 30. May, Albert; and Witt, W. R., Jr.: Free-Flight Determinations of the Drag Coefficients of Spheres. J. Aero. Sci., vol. 20, no. 9, Sept. 1953, pp. 635-638.
- 31. Hodges, A. J.: The Drag Coefficient of Very High Velocity Spheres. J. Aero. Sci., vol. 24, no. 10, Oct. 1957, pp. 755-758.
- 32. Emmons, Howard W., ed.: Fundamentals of Gas Dynamics. Vol. III of High Speed Aerodynamics and Jet Propulsion. Princeton Univ. Press, c.1958.
- 33. Charters, A. C.; and Thomas, R. N.: The Aerodynamic Performance of Small Spheres From Subsonic to High Supersonic Velocities. Jour. Aero. Sci., vol. 12, no. 4, Oct. 1945, pp. 468-476.
- 34. Rouse, Hunter: Elementary Mechanics of Fluids. John Wiley & Sons, Inc., c.1946, p. 245.
- 35. Kavanau, L. L.: Heat Transfer From Spheres to a Rarefied Gas in Subsonic Flow. Trans. ASME, vol. 77, no. 5, July 1955, pp. 617-623.
- 36. Barnett, Henry C.; and Hibbard, Robert E., eds.: Basic Considerations in the Combustion of Hydrocarbon Fuels With Air. NACA Rept. 1300, 1957.
- 37. Brokaw, Richard S.: Alignment Charts for Transport Properties Viscosity, Thermal Conductivity, and Diffusion Coefficients for Nonpolar Gases and Gas Mixtures at Low Density. NASA TR R-81, 1961.
- 38. Svehla, Roger A.: Estimated Viscosities and Thermal Conductivities of Gases at High Temperatures. NASA TR R-132, 1962.
- 39. Reid, Robert C.; and Sherwood, Thomas K.: The Properties of Gases and Liquids. McGraw-Hill Book Co., Inc., 1958, p. 226.





40. FitzGibbon, Sheila A.: Real Gas Supersonic Flow Field Solutions in the Shock Layer Around a 9° Sphere-Cone at Mach = 20.4, 21.4, and 21.2. Aerodyn. Data Mem. No. 1:48, Missile and Space Vehicle Dept., Gen. Elec. Co., May 1961.

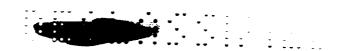
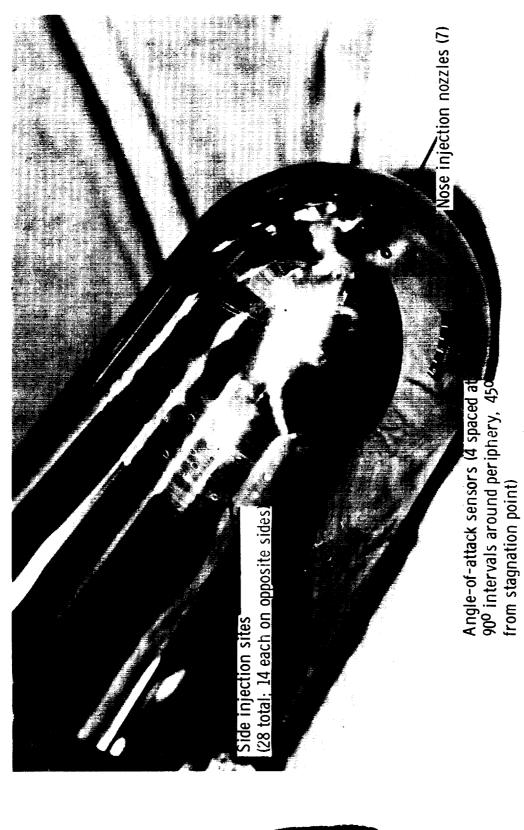


TABLE I.- PROPERTIES OF NONCHARRING ABLATION MATERIAL

ρ,	lb,	$/ft^3$.			•	•	•	•		•	•		•			•			٠		•	•		•										63
с,	Βtι	u/lb-°I	ī	•	•	•	•	•	•	•	•		•	•	•	•		•	•		•	•	•	•				•			•	•	•	0.43
k,	Btı	u/hr-ft	;_O	F	•	•	•	•	•	•	•	•	•	•	•	•	•	•	•	•	•	•	•	•	•	•	•	•	•	•	•	•	•	0.09
He	ľf,	Btu/1)	•	•	•	•	•	•	•	•	•	•	•	•	•	•	•	•	•	•	•	•	•	•	2	25C) +	- ().5	5(I	Iav	, -	350)
ṁ,	lb,	/sec - ft	;2	•	•	•	•	•	•	•	•		•			•	•	•	•	•	(0.3	39E	} >	< J	LOS) _e	xp	,(-).3	376 T	x ab	105



L-62-6951.1 Figure 1.- Photograph of beryllium nose section of RAM B2 flight vehicle showing nose and side injection sites.



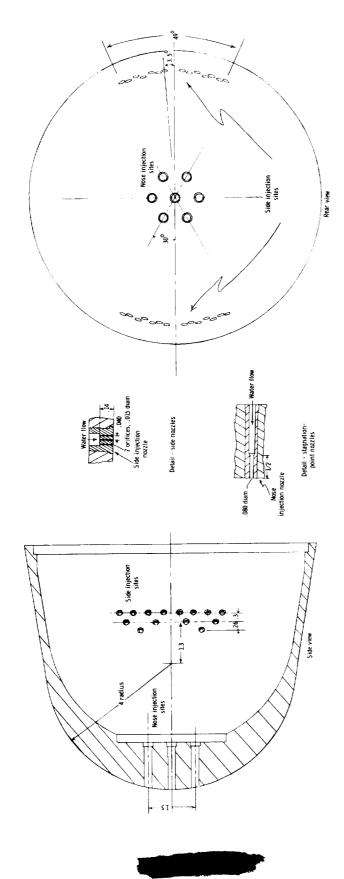


Figure 2.- Exact location and arrangement of side and nose injection sites and details of injection nozzles. All dimensions in inches.

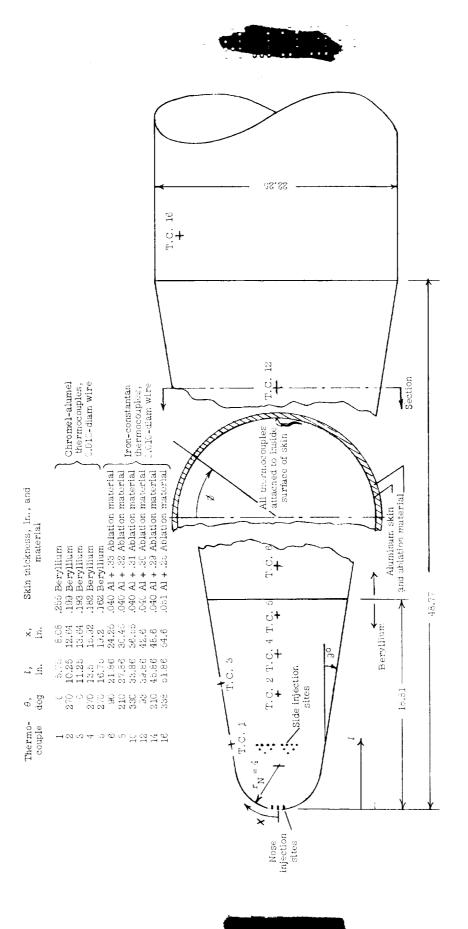


Figure 5.- Side-view sketch of forward portion of vehicle showing thermocouple locations in relation to side injection sites. All dimensions in inches.



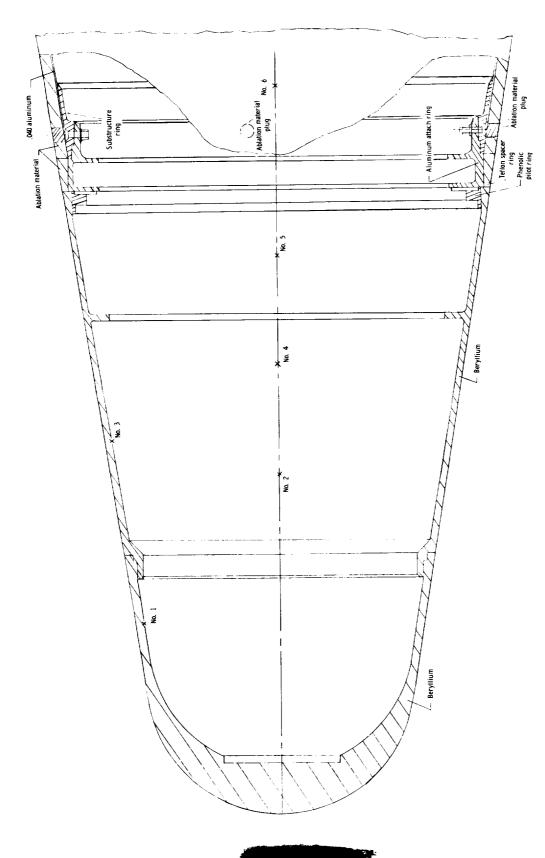
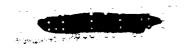


Figure 4.. Sectional drawing of beryllium nose cone showing thermocouple locations in relation to joints and flanges.



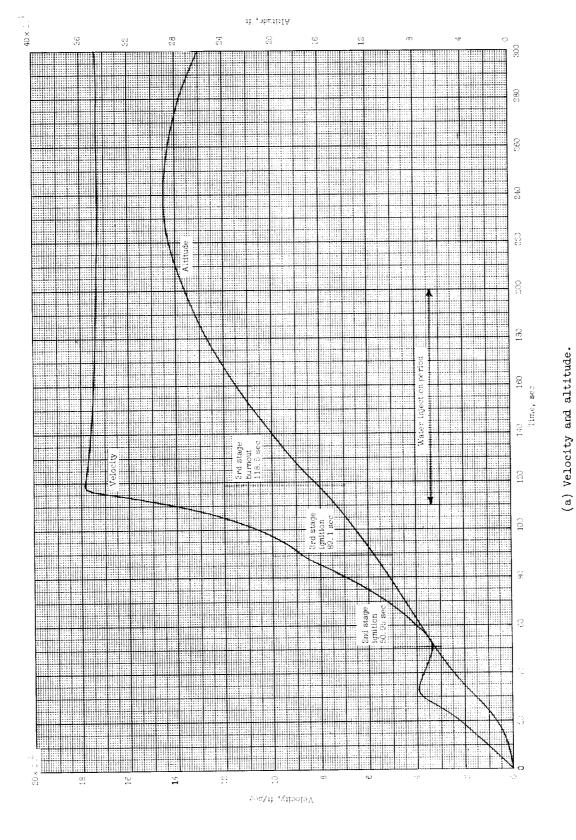
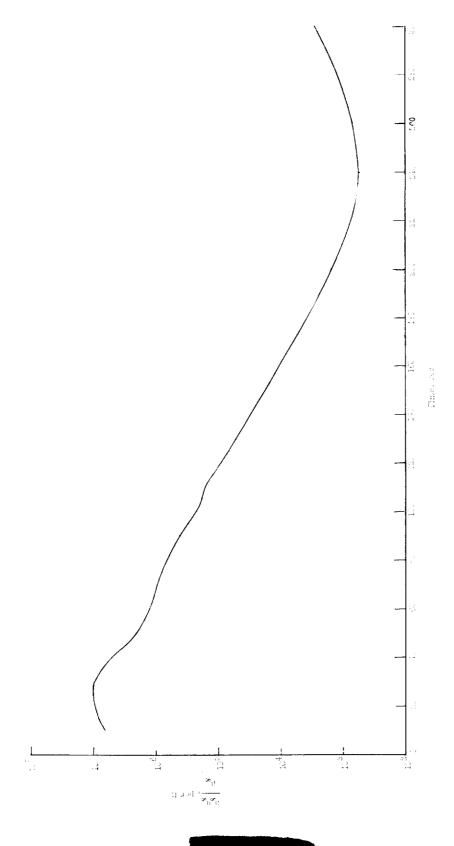


Figure 5.- Trajectory parameters for RAM B2 flight.

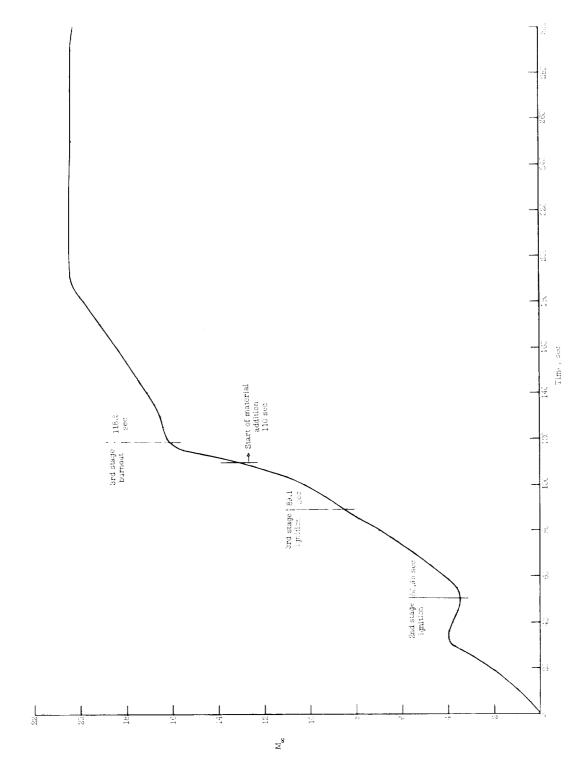




(b) Free-stream Reynolds number per foot.

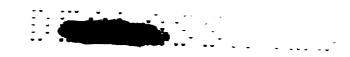
Figure 5.- Continued.





(c) Free-stream Mach number.

Figure 5.- Concluded.



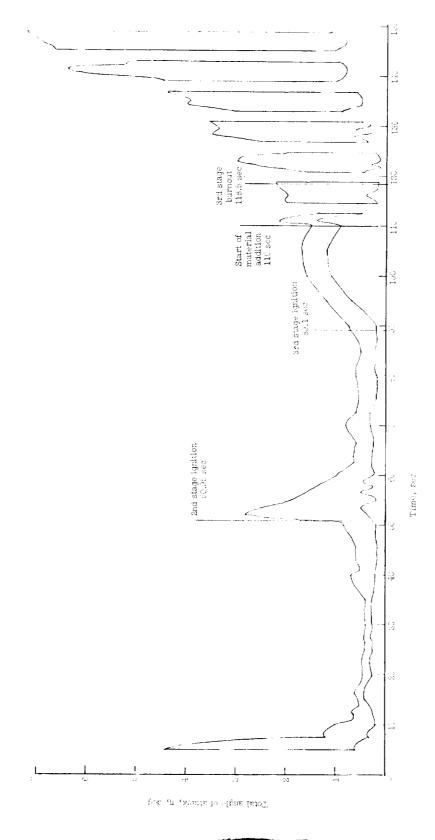
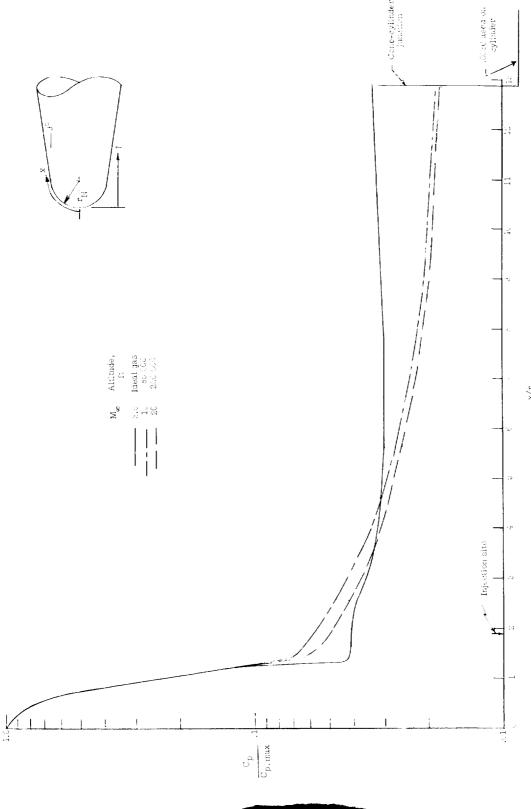


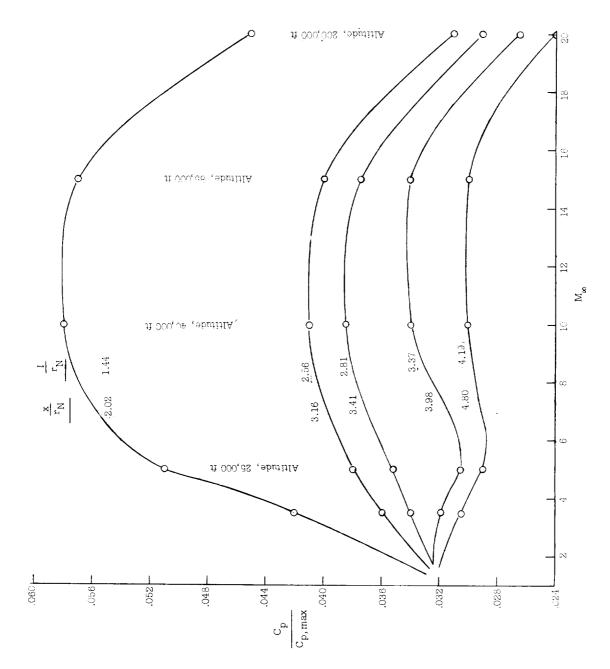
Figure 6.- Envelope of maximum and minimum total angle of attack for the RAM B2 flight (from ref. 4).





(a) Typical variation with $x/r_{
m N}$ at different Mach numbers.

Figure 7.- Theoretical pressure distributions for a sphere-cone from flow-field solutions of reference 9.



(b) Variation with stream Mach number at axial station corresponding to thermocouple numbers 1 through 5.

Figure 7.- Concluded.



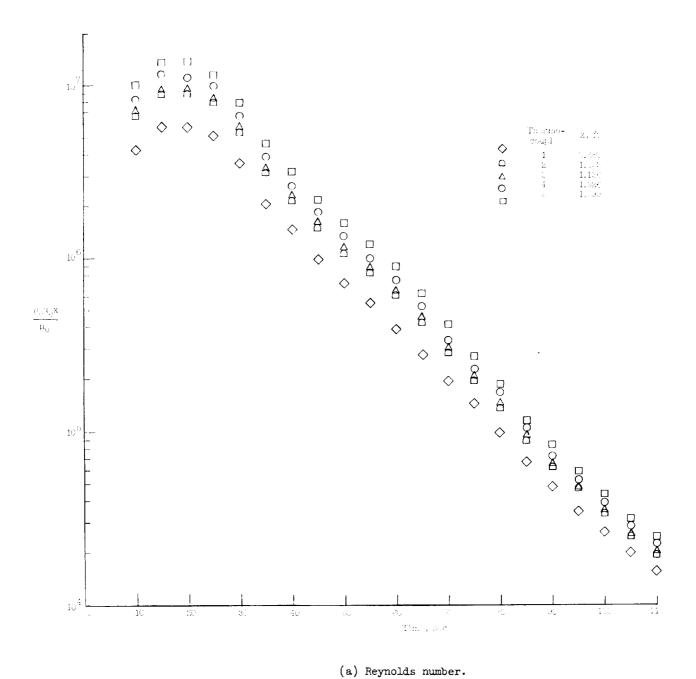


Figure 8.- Local flow conditions for the five thermocouple positions on the beryllium nose.

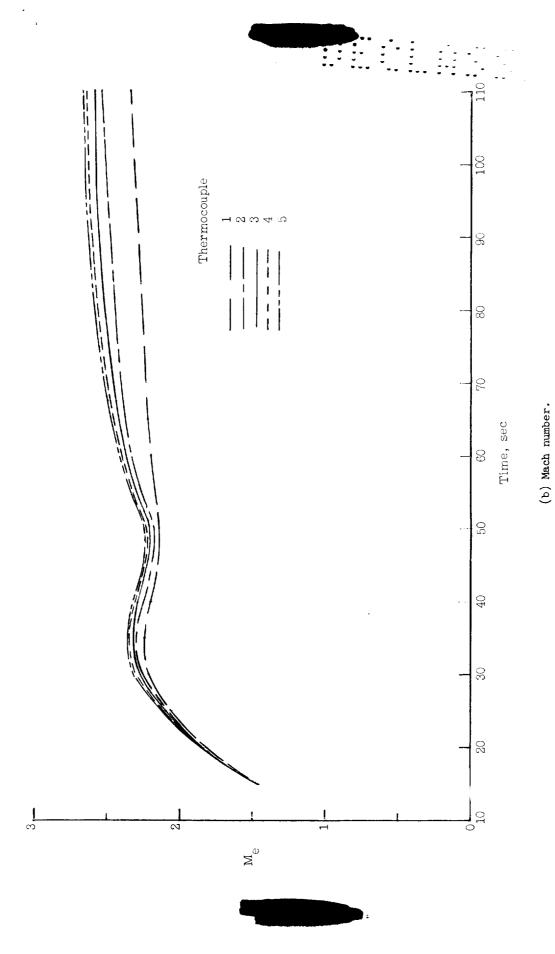
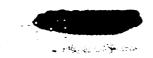
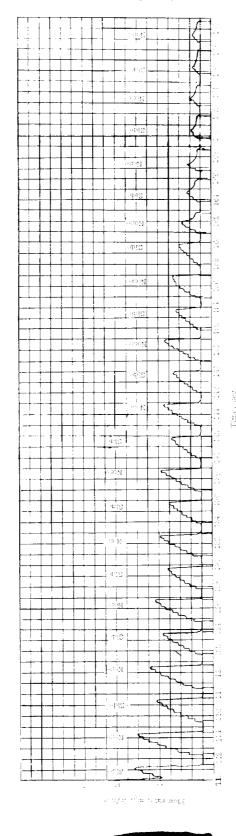


Figure 8.- Concluded.





marker 12 to the second second

Figure 9.- Variation of total water flow rate with time.



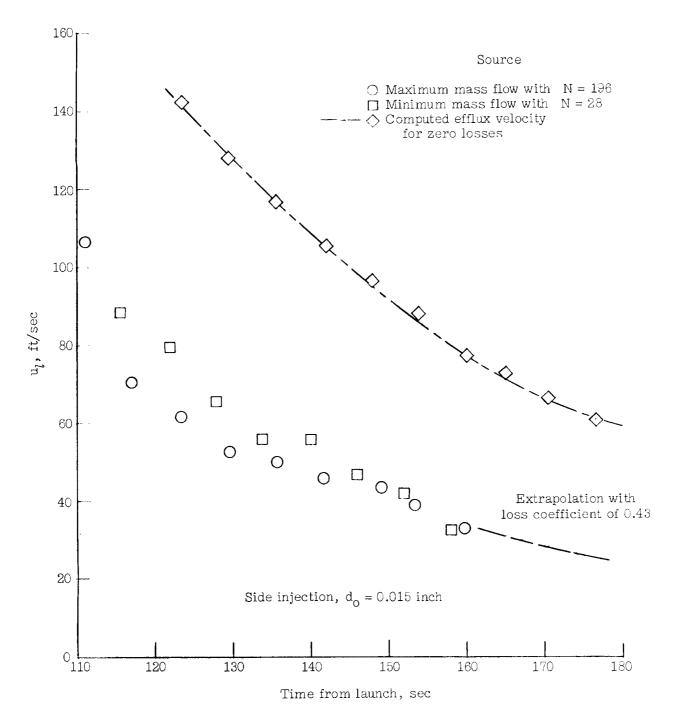


Figure 10.- Water efflux velocity at exit of orifices. Line faired to points computed from measured tank pressure assuming no losses.





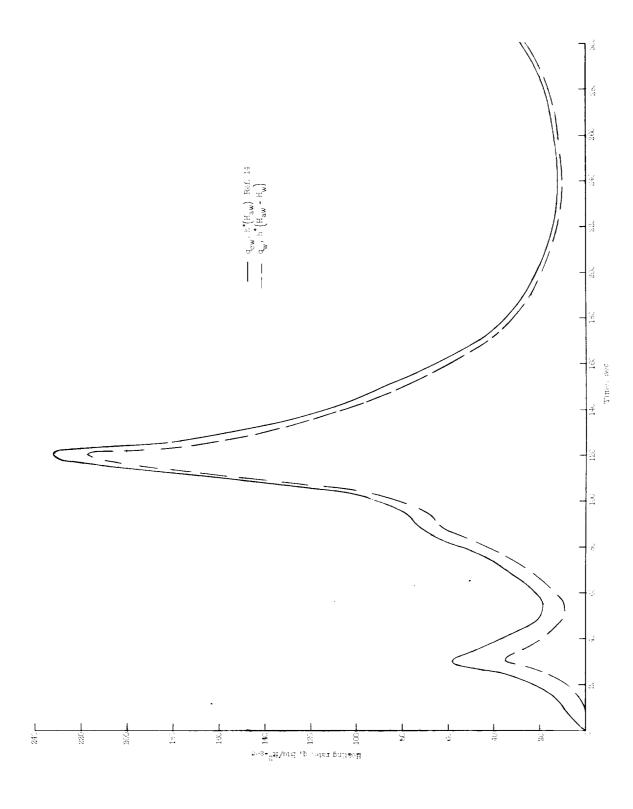


Figure 11.- Input values of cold-wall q and resulting aerodynamic q for the stagnation point with zero injection.

Beryllium wall, 1.5 inches thick.



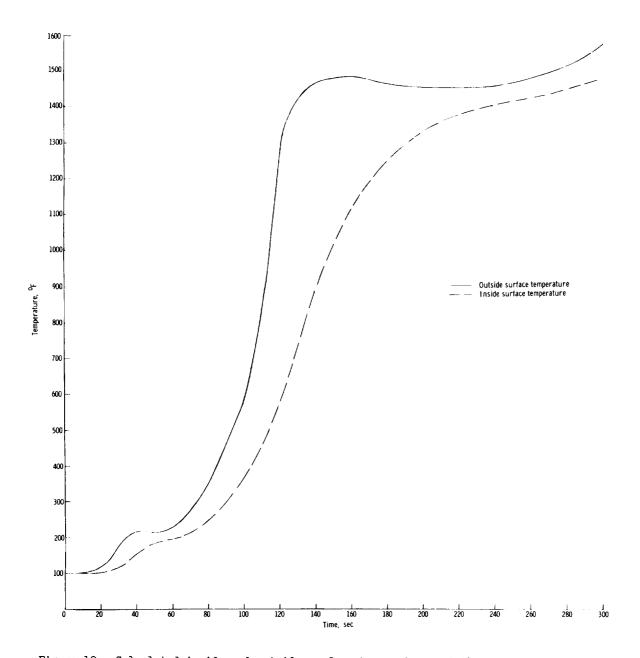


Figure 12.- Calculated inside and outside surface temperatures at the stagnation point using the aerodynamic $\, {\bf q} \,$ from figure 11.





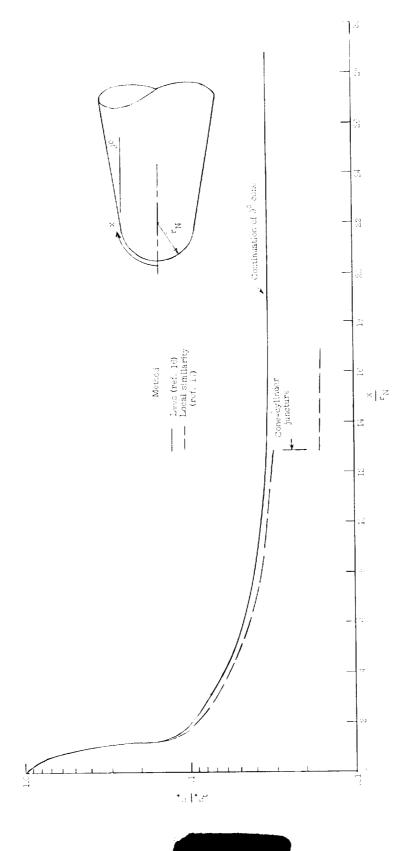


Figure 13.- Theoretical laminar heat-transfer coefficient distribution on sphere-cone. Nominal conditions used were: $\mu_{\rm w}=19~500~{\rm ft/sec}$; altitude = 200 000 ft; $\Gamma_{\rm w}=1500^{\rm o}$ R; pressure distribution from $C_{\rm p}/C_{\rm p,max}$ for M_w = 15, figure 7.

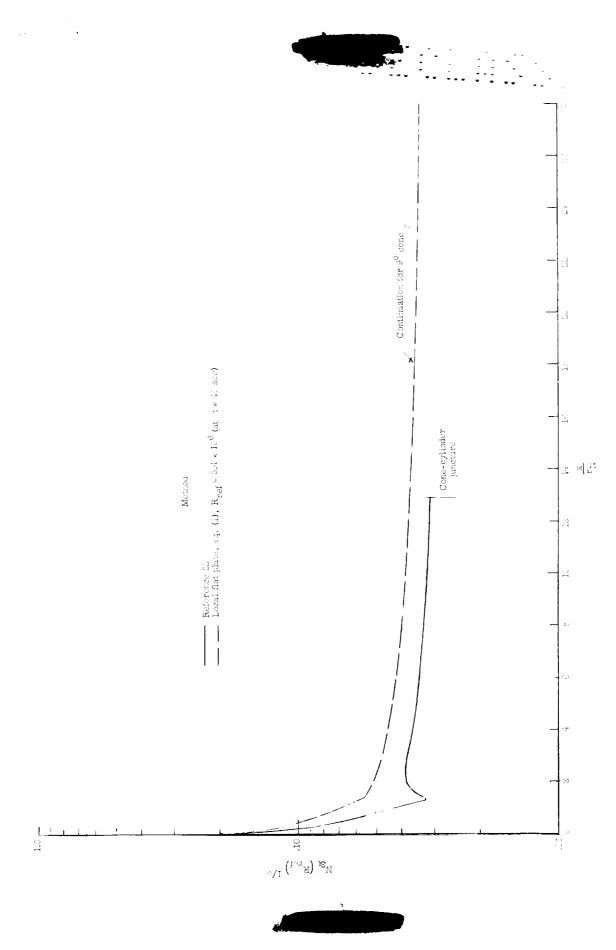
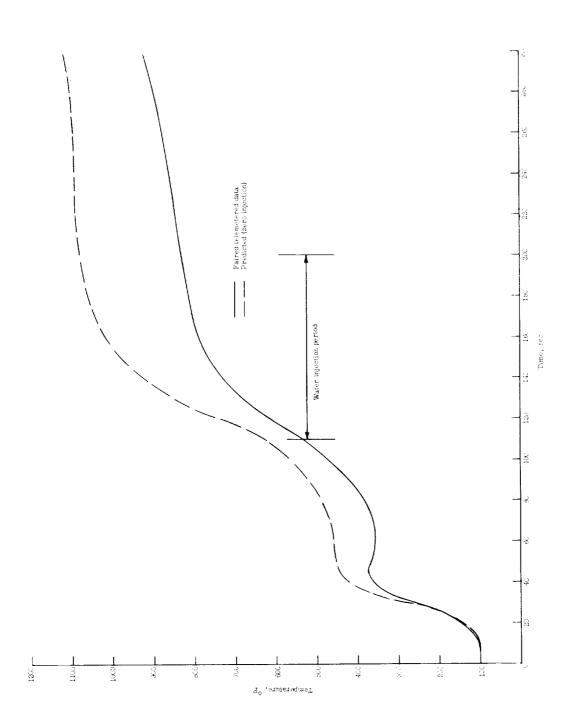


Figure 14.- Theoretical distribution of turbulent heat-transfer parameter on sphere-cone. Nominal conditions used were: $M_{\infty} = 4.0$; $T_{\omega} = 660^{\circ}$ R; $T_{\infty} = 400^{\circ}$ R.

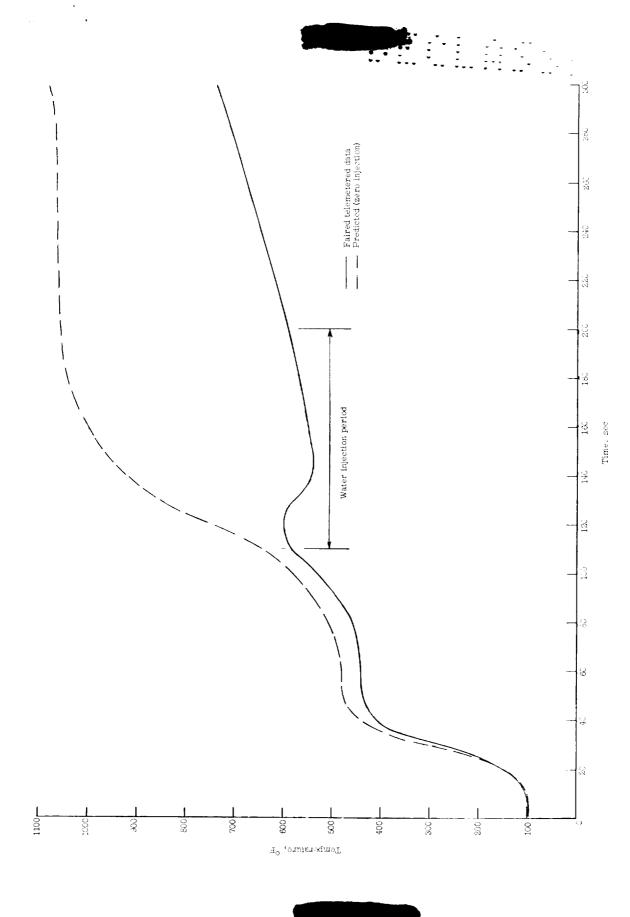




The State of the S

(a) Thermocouple 1; l = 5.75 in.; $\phi = 0^{\circ}$.

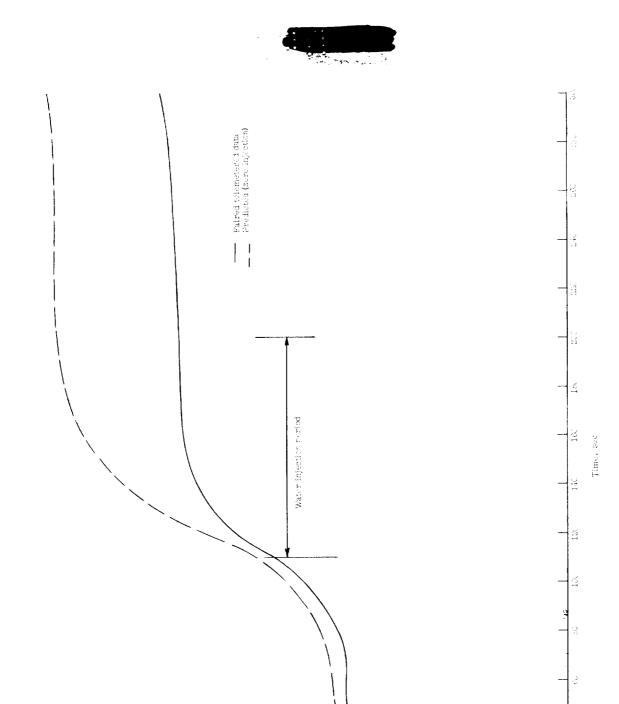
Figure 15.- Comparison of measured inside wall temperatures on beryllium nose with predicted values for no injection. Turbulent heating from equation (1) was assumed up to 50 seconds; from this time on laminar heating was assumed.



(b) Thermocouple 2; l = 10.25 in.; $\phi = 270^{\circ}$.

Figure 15.- Continued.

61



Ž T

3

H^o townstregmeT

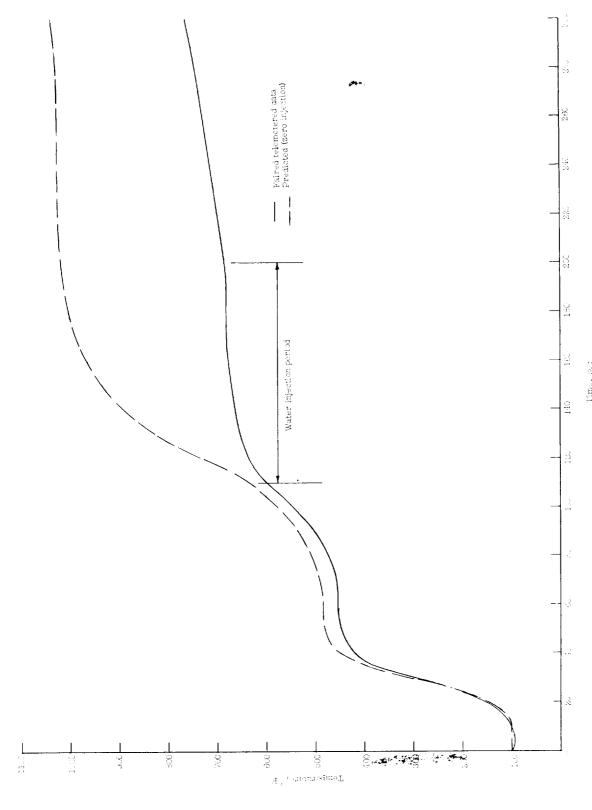
33

(c) Thermocouple 5; l = 11.25 in.; $\phi = 0^{\circ}$.

Figure 15.- Continued.

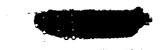
1100

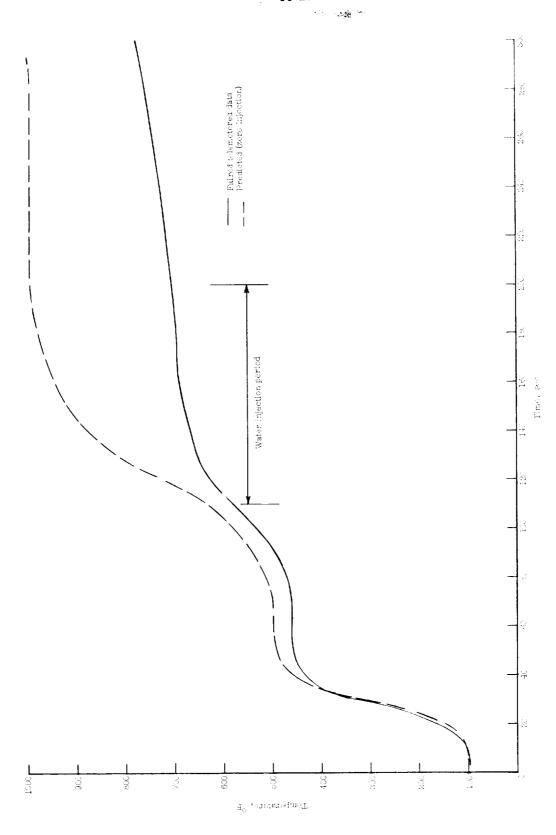




(d) Thermocouple μ_{i} , l=15.5 in.; $\phi=270^{\circ}$.

Figure 15.- Continued.





(e) Thermocouple 5; $l = 16.75 \text{ in.}; \ \phi = 270^{\circ}.$

Figure 15.- Concluded.



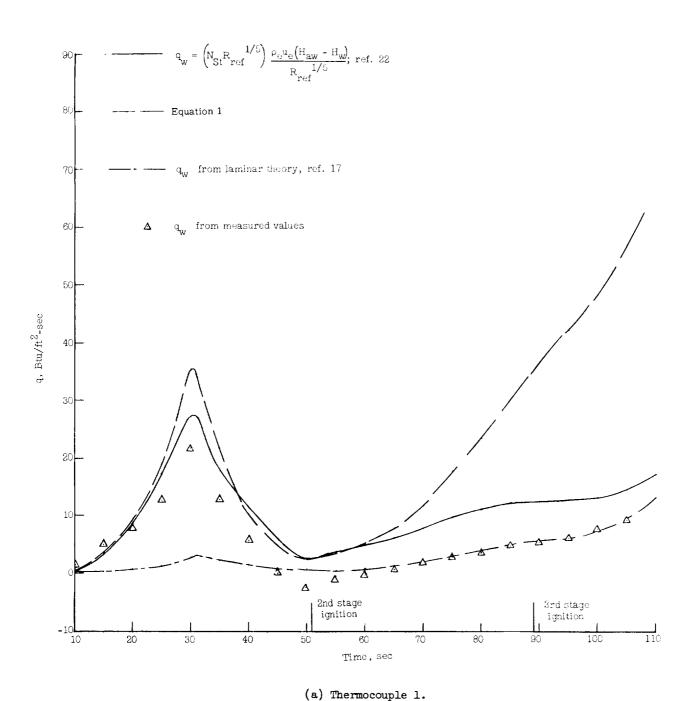
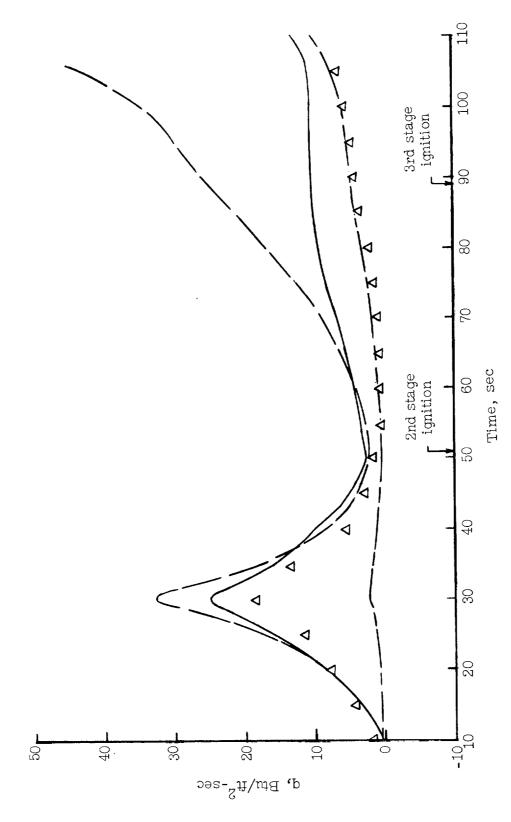


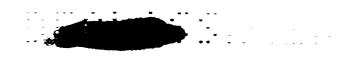
Figure 16.- Comparison of experimental heating rates obtained on the beryllium nose before the water injection period with calculated values from laminar and turbulent formulas.





(b) Thermocouple 2.

Figure 16.- Continued.



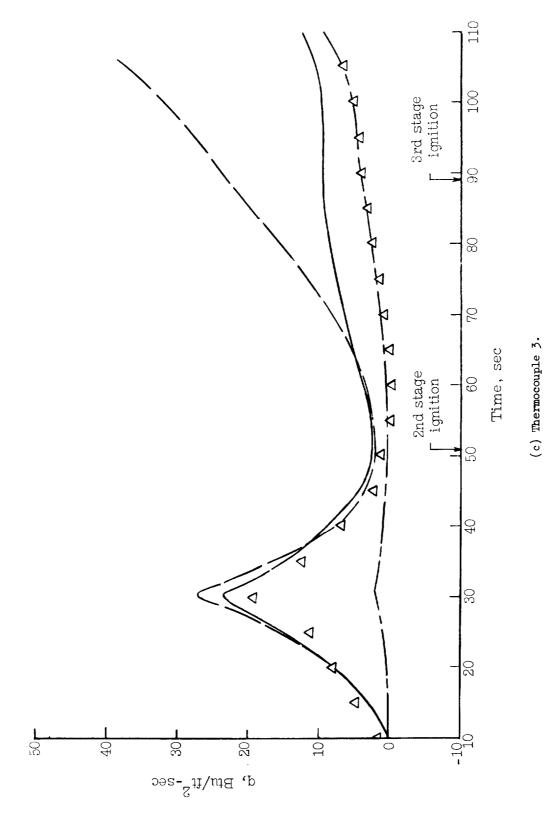
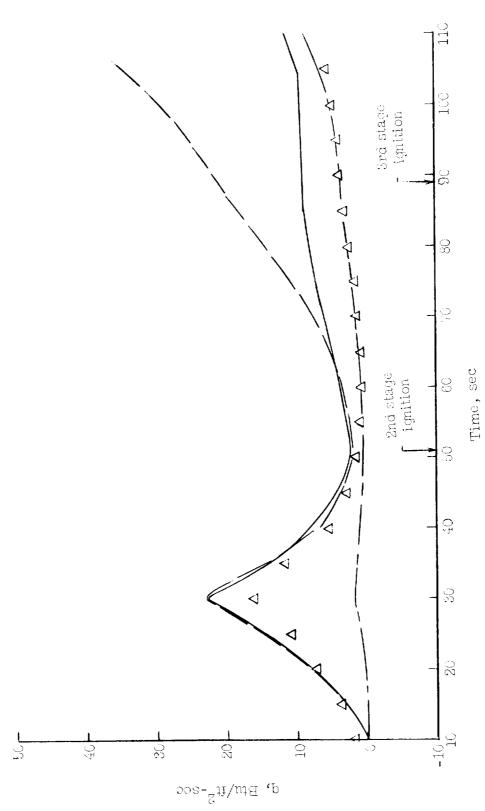


Figure 16.- Continued.

67

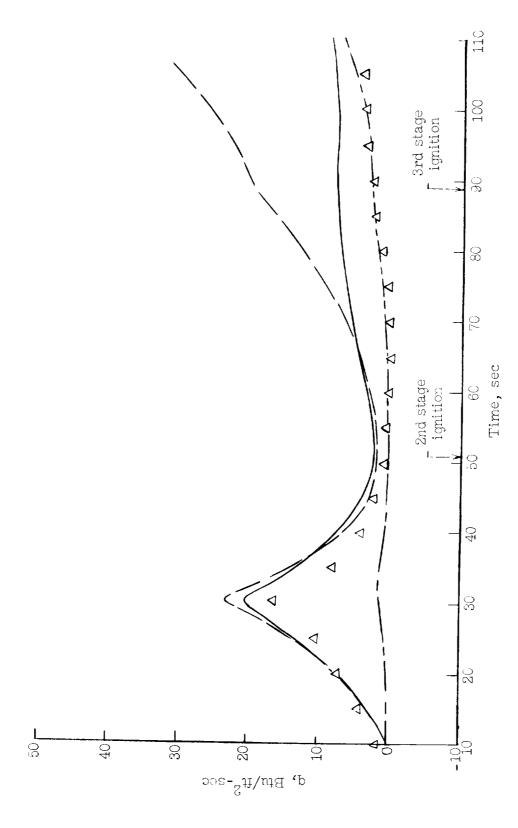




(d) Thermocouple 4.

Figure 16.- Continued.





(e) Thermocouple 5.

Figure 16.- Concluded.

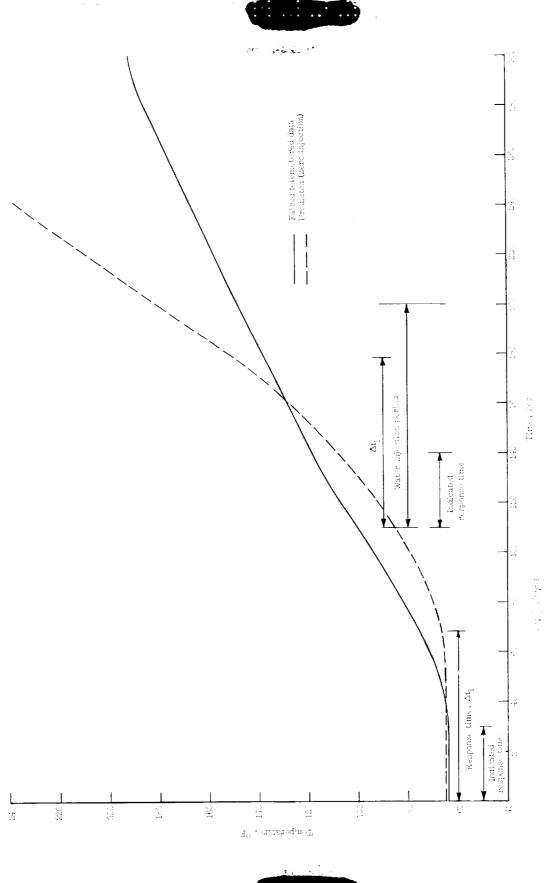
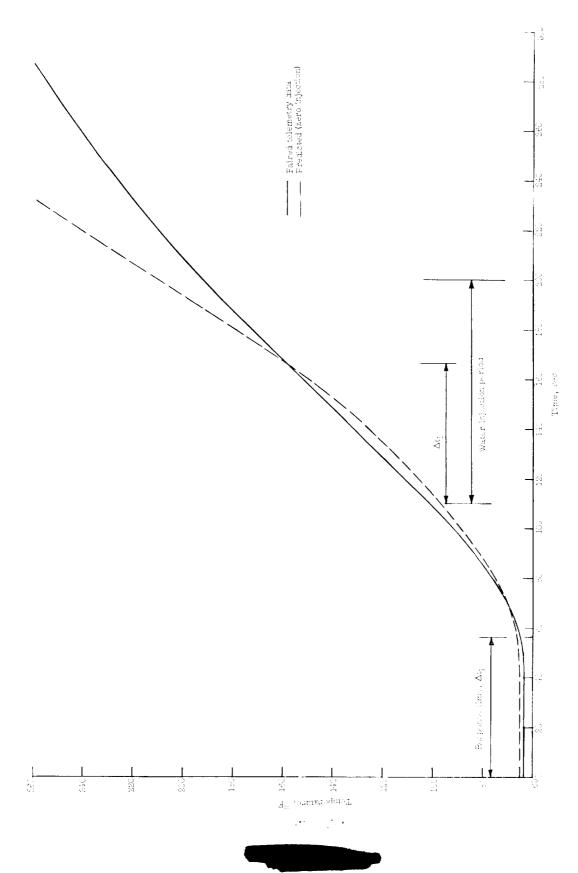


Figure 17.- Measured and predicted temperatures at inside surface of the composite wall.

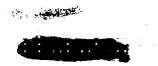
(a) Thermocouple 6; 0.35-inch-ablation material plus 0.04-inch aluminum.

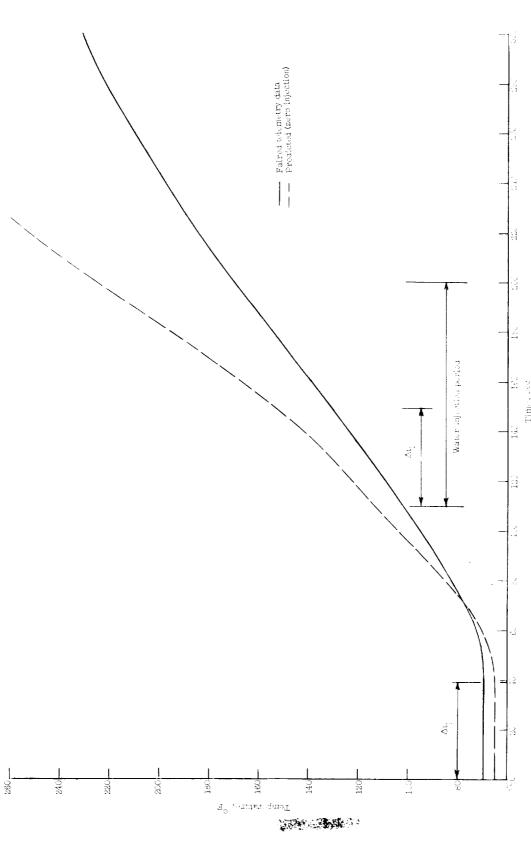




(b) Thermocouple 12; 0.30-inch-ablation material plus 0.04-inch aluminum.

Figure 17.- Continued.





(c) Thermocouple 16; 0.25-inch-ablation material plus 0.051-inch aluminum.

Figure 17.- Concluded.

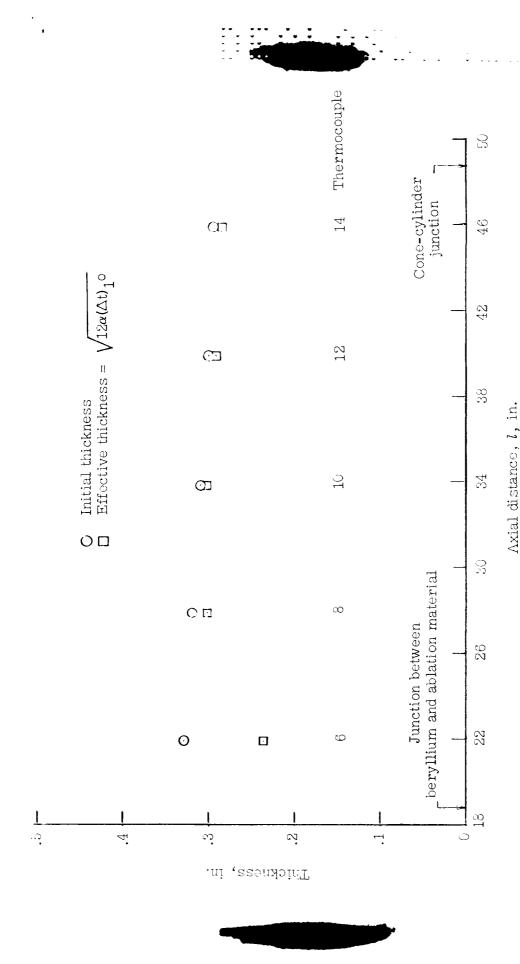


Figure 18.- Comparison of actual initial thickness of ablation material on conical portion of vehicle with effective thickness deduced from observed response time.



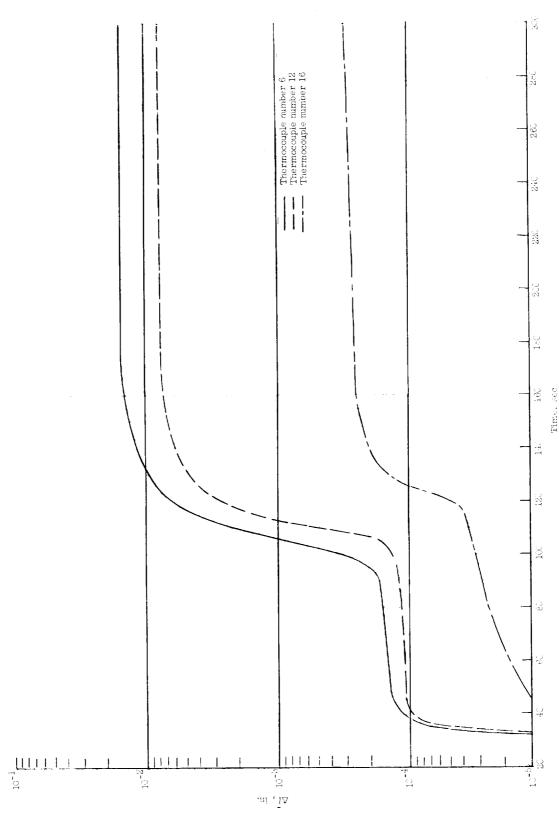
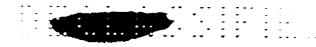
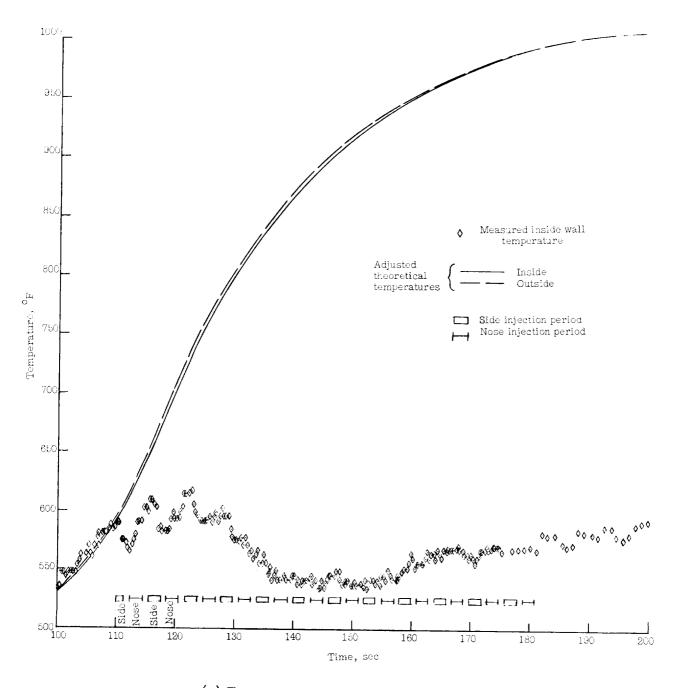


Figure 19.- Predicted amount of material ablated at three positions on vehicle.



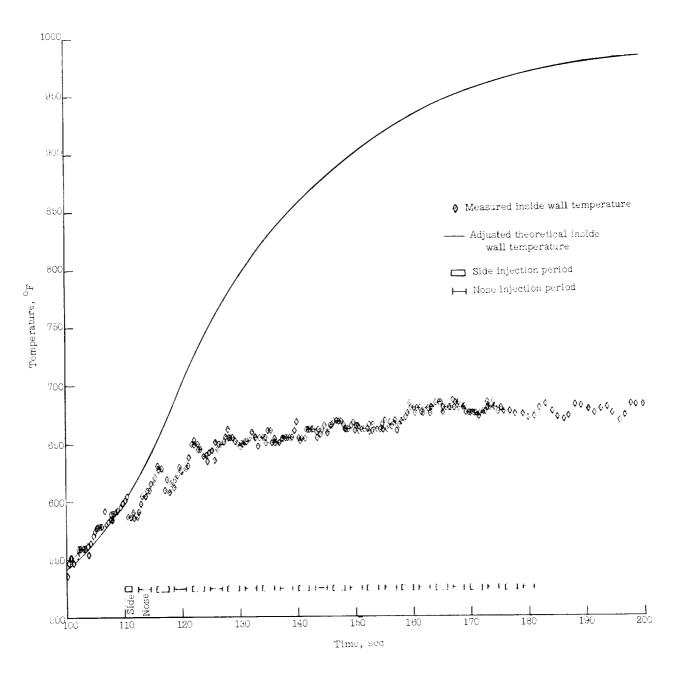


(a) Thermocouple 2; l = 10.25 in.; $\phi = 270^{\circ}$.

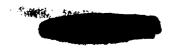
Figure 20.- Effect of water injection on inside wall temperature of beryllium nose from telemetered data points. Temperature curves have been adjusted to coincide with the data at 110 seconds.



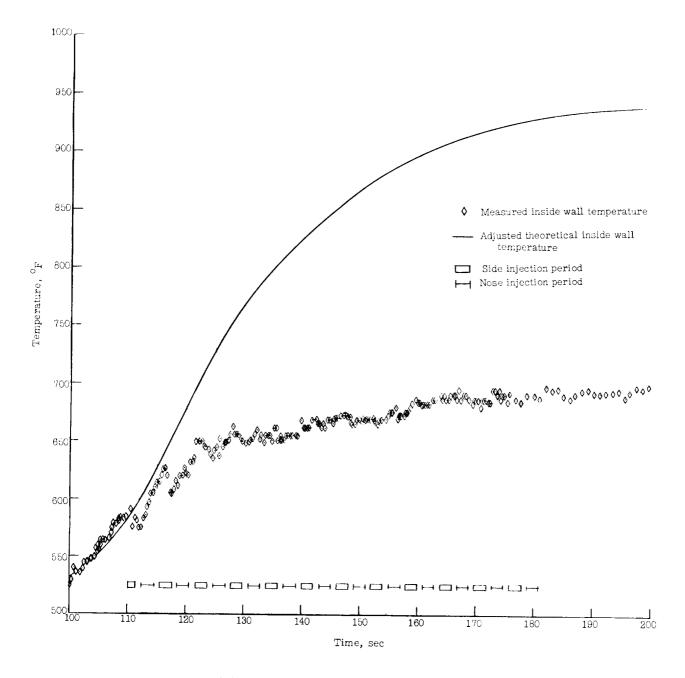




(b) Thermocouple 4; l = 13.50 in.; $\phi = 270^{\circ}$. Figure 20.- Continued.





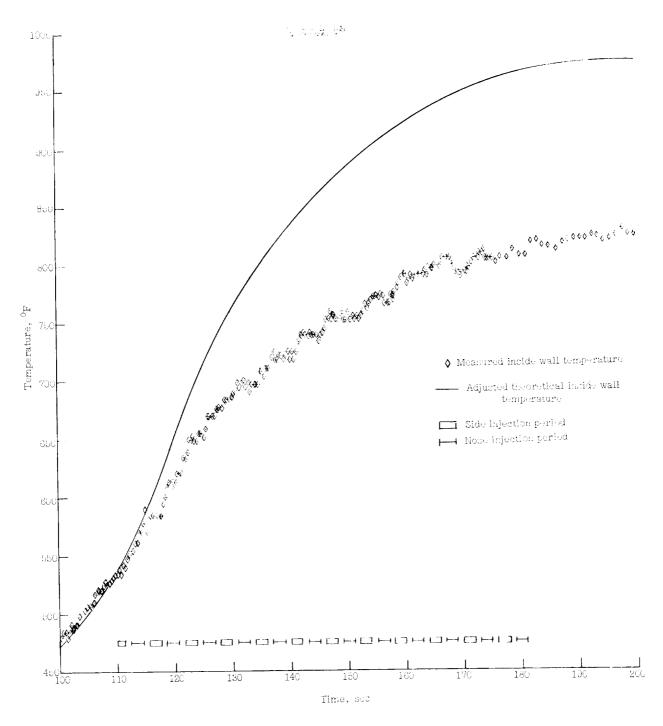


(c) Thermocouple 5; l = 16.75 in.; $\phi = 270^{\circ}$.

Figure 20.- Continued.



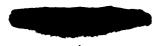




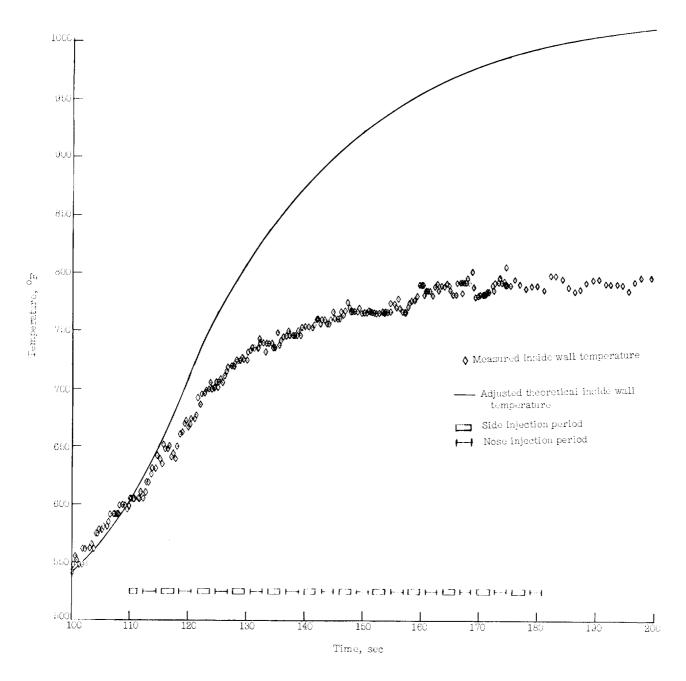
(d) Thermocouple 1; l = 5.75 in.; $\phi = 0^{\circ}$.

Figure 20.- Continued.

78







(e) Thermocouple 3; l = 11.25 in.; $\emptyset = 0^{\circ}$.

Figure 20.- Concluded.

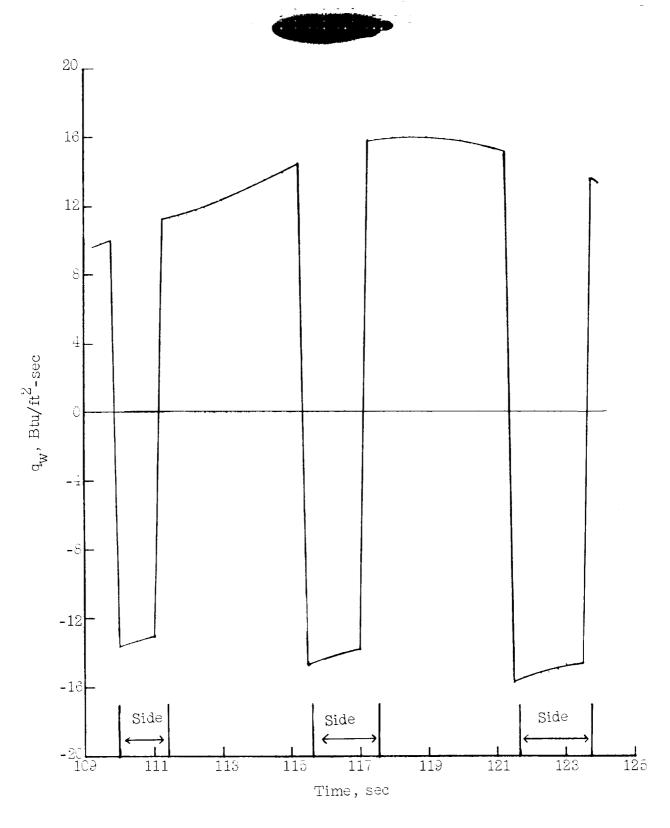


Figure 21.- Assumed aerodynamic heating values used to ascertain thermal response of beryllium.



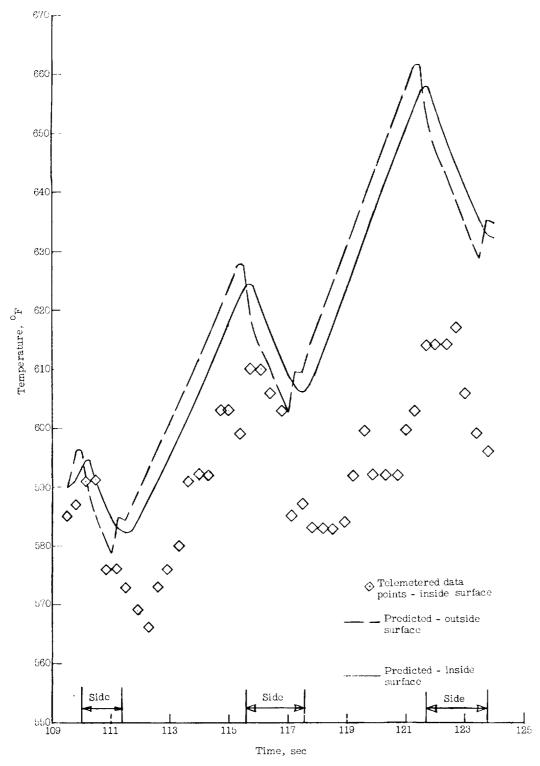
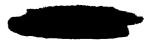
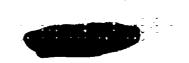


Figure 22.- Comparison of wall temperature history computed from heating-rate variation of figure 21 with telemetered data points from thermocouple 2.





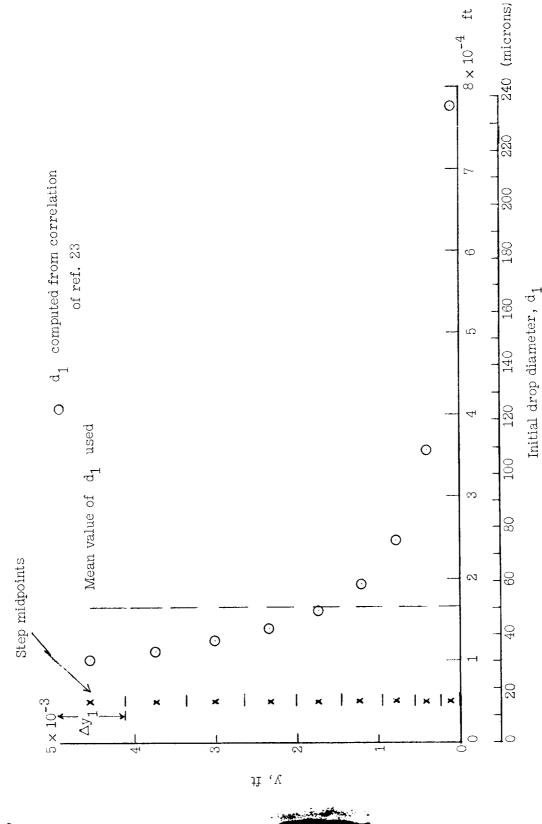


Figure 23.- Variation of initial water drop diameter dl and step size Ay with distance from surface as used in calculations for conditions at 115 seconds.

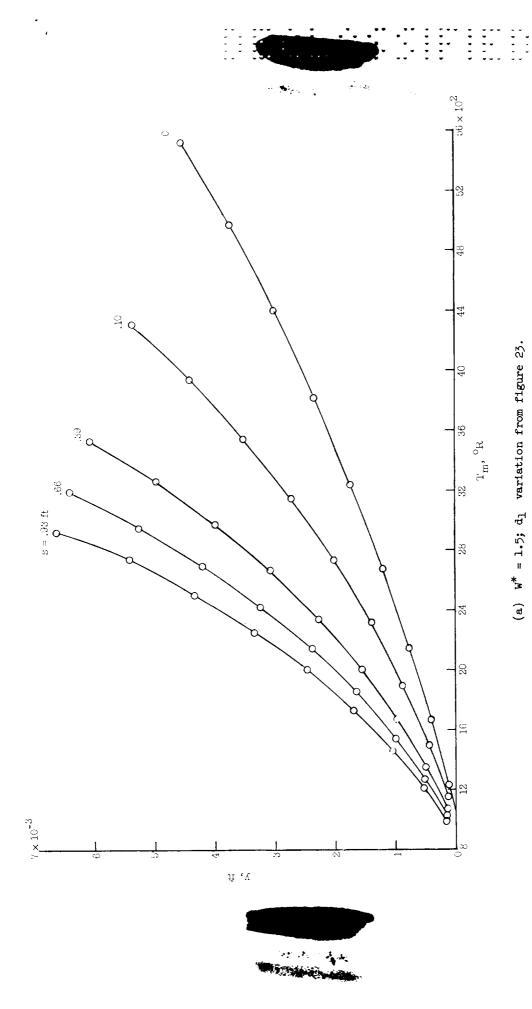
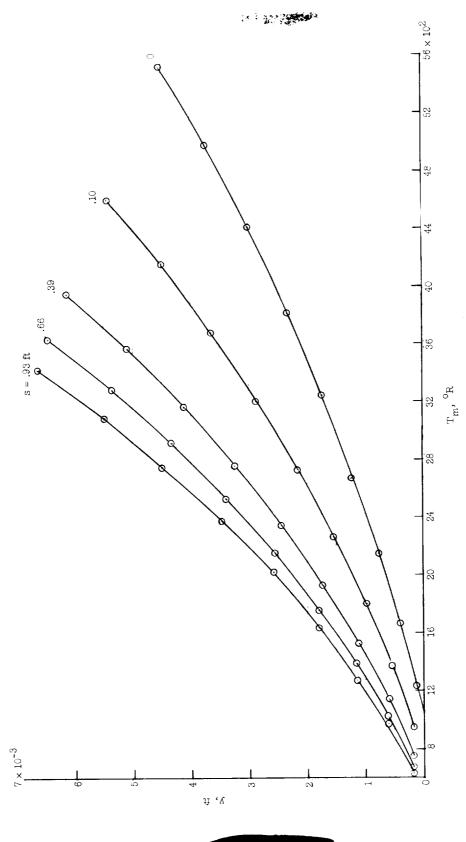


Figure 24.- Computed effect of water evaporation on temperature profile near surface at four distances from injection site (S = 0). Trajectory time, 115 seconds; (Te) $_{\rm s=0}$ = 75000 R.

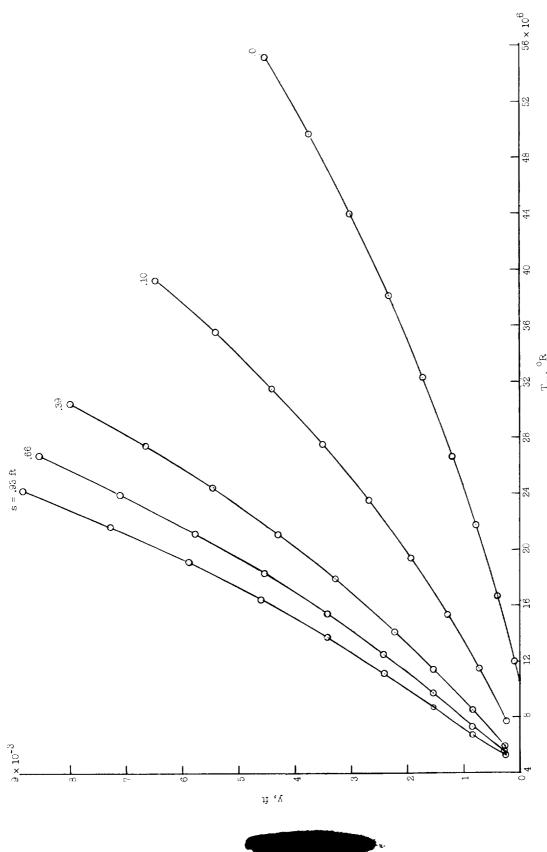
(a) $W^* = 1.5$; d_1 variation from figure 23.



(b) $W^* = 1.5$; $d_1 = 50$ microns, constant.

Figure 24.- Continued.

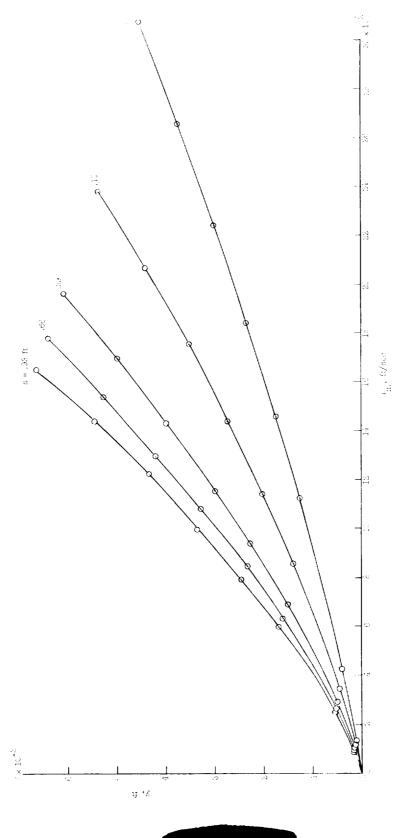




(c) $W^* = 3.0$; $d_1 = 50$ microns, constant.

Figure 24.- Concluded.

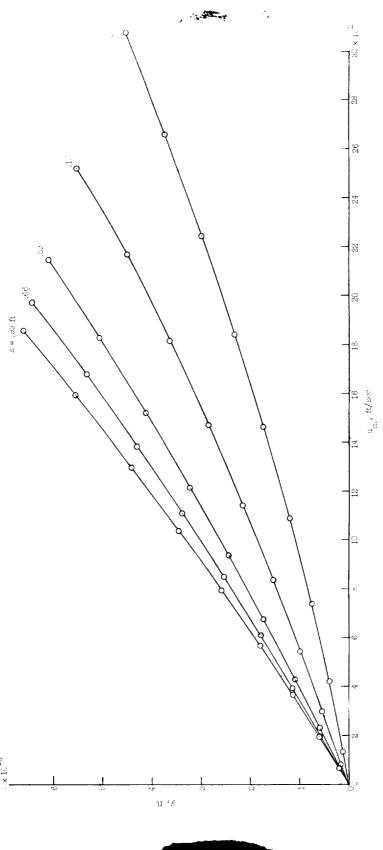




(a) $W^* = 1.5$; d₁ variation from figure 25.

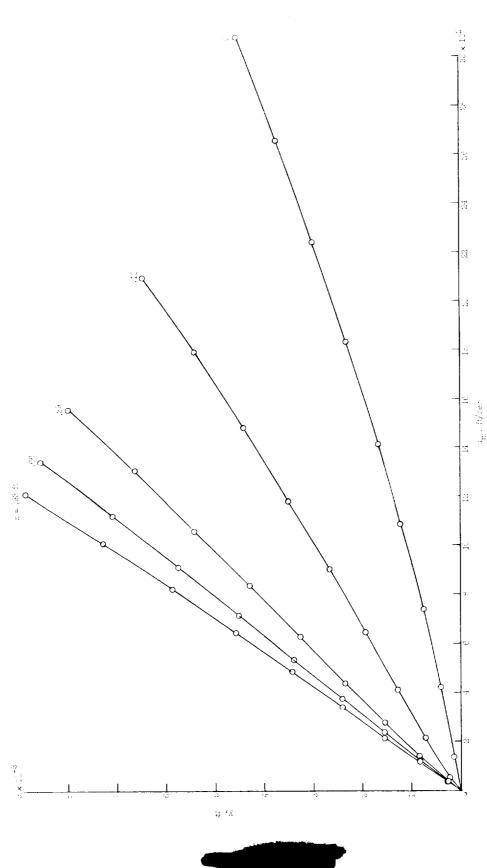
Figure 25.- Computed effect of water evaporation on velocity profiles. Trajectory time, 115 seconds; $(u_e)_{s=0} = 10\ 100\ ft/sec$.





(b) $W^* = 1.5$; $d_1 = 50$ microns, constant. Figure 25.- Continued.

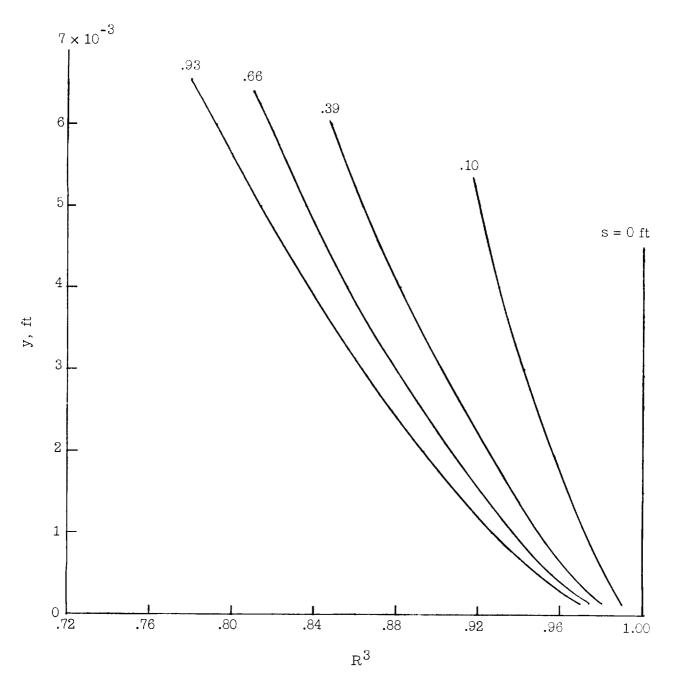




(c) $W^* = 5.0$; $d_1 = 50$ microns, constant.

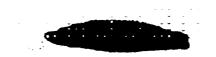
Figure 25.- Concluded.

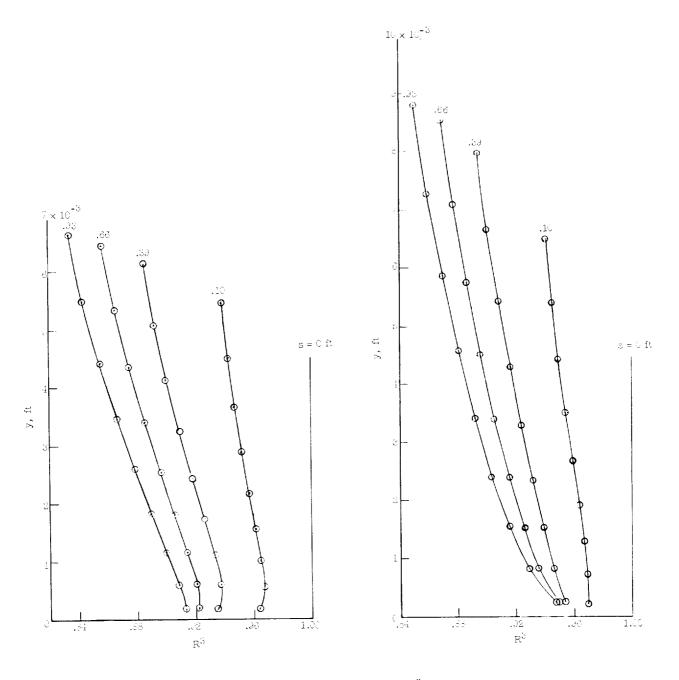




(a) $W^* = 1.5$; d_1 variation from figure 23.

Figure 26.- The variation with distance from the surface of the fraction of injected water still in liquid form. Trajectory time, 115 seconds.





(b) $W^* = 1.5$; $d_1 = 50$ microns, constant.

(c) $W^* = 3.0$; $d_1 = 50$ microns, constant.

Figure 26.- Concluded.



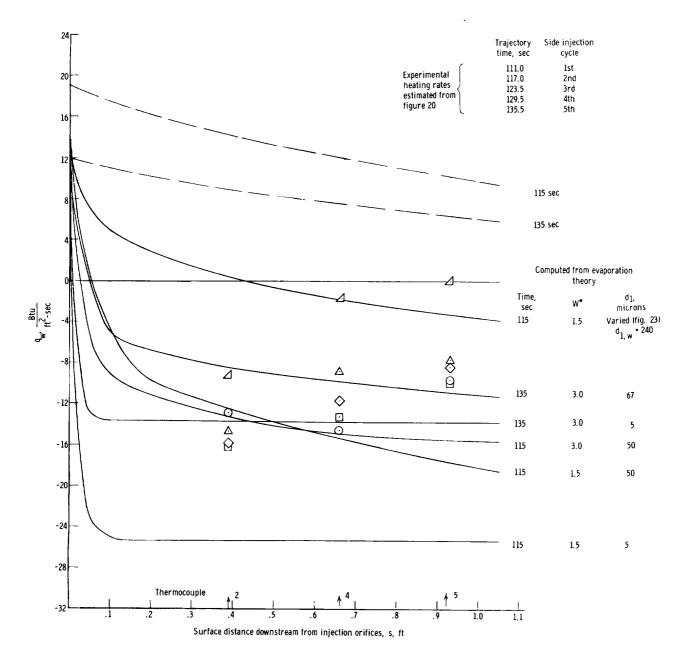


Figure 27.- Comparison of the effect of water injection on surface heat transfer as estimated from the flight data and as computed from the evaporation theory.



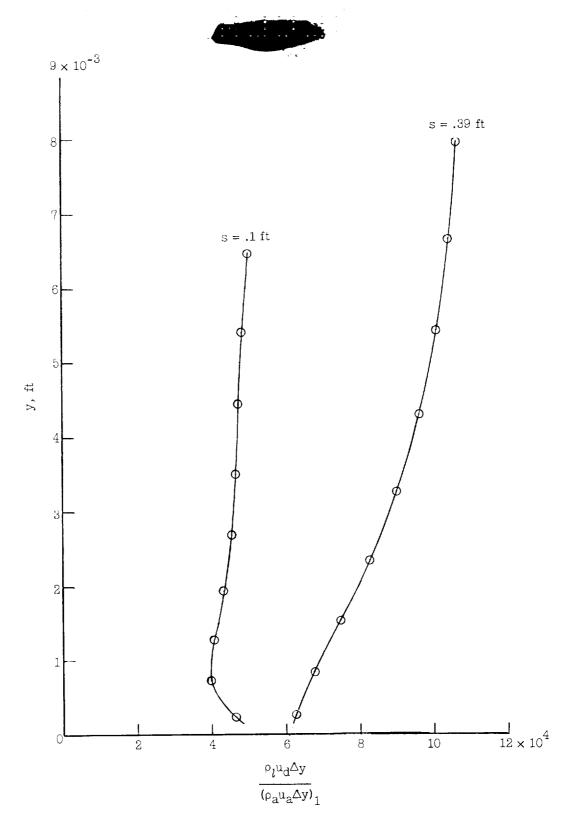


Figure 28.- Variation in boundary layer of factor in droplet concentration equation (A37).



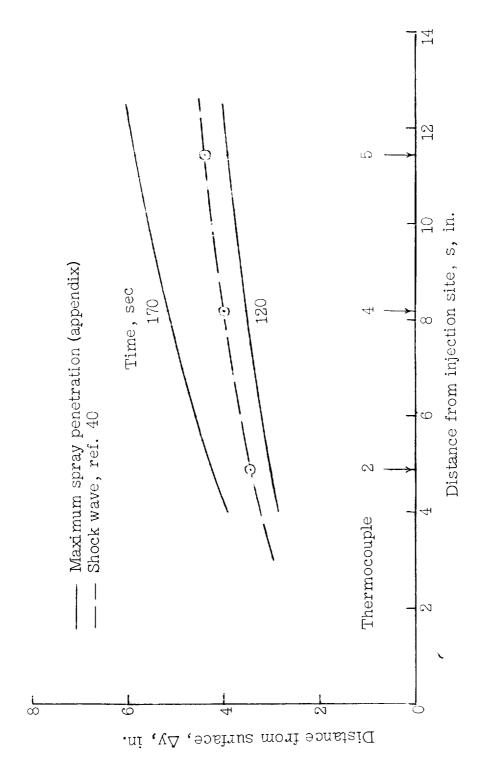


Figure 29.- Calculated maximum spray penetration and shock-wave location for RAM B2 flight.



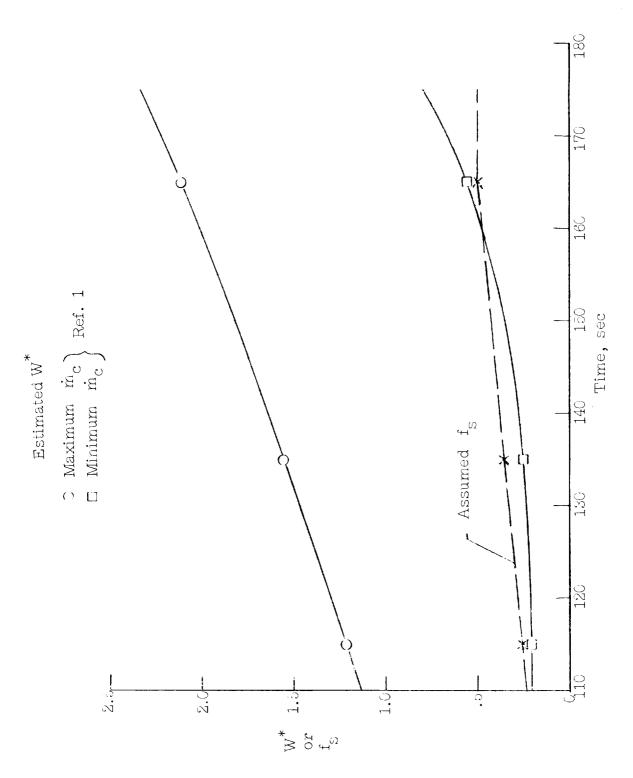


Figure 30.- Estimated values of W* for inviscid flow field at thermocouple 2. Based on fs variation shown.